U.S. DEPARTMENT OF ENERGY | Office of Science

DOE/SC-ARM-TR-277

Aerosol Inlets for a Mid-Sized Uncrewed Aerial System (UAS)

MS Pekour MK Newburn

April 2022

ARM

DISCLAIMER

DOE/SC-ARM-TR-277

Aerosol Inlets for a Mid-Sized Uncrewed Aerial System (UAS)

MS Pekour
MK Newburn
Both at Pacific Northwest National Laboratory

April 2022

Work supported by the U.S. Department of Energy,
Office of Science, Office of Biological and Environmental Research

Executive Summary

The purpose of this technical report is to document the efforts to design and test two inlet systems for aerosol sampling suitable for deployment on a medium-sized fixed-wing Uncrewed Aerial System (UAS).

This work, which was supported by the U.S. Department of Energy's Atmospheric Radiation Measurement (ARM) user facility, was conducted at the Pacific Northwest National Laboratory (PNNL) for the ARM Aircraft Facility (AAF) starting in November 2017. The current work is a part of AAF efforts to instrument the ArcticShark (a mid-sized UAS owned and operated by the AAF) for atmospheric research and develop a scientific payload for deployment on a similar-sized UAS with minimal adaptation and integration.

An aerosol inlet system is necessary to sample and transport ambient air samples to the scientific instrumentation with minimal distortions to the aerosols. Two isokinetic aerosol inlets were designed: the first is a simple passive system for a single instrument suitable to be installed in a wing pylon; the second is a system with active control designed to sample and distribute air among several heterogeneous instruments and to provide basic humidity control of the air sample so that the measured aerosol parameters should correspond to "dry" conditions (a common requirement). Both systems could be easily adapted for deployment on another platform and/or with a different set of instrumentation. Several conducted flight tests showed that the inlets' performance met our design goals.

Acknowledgments

The authors wish to thank the many people who helped conduct various tests. We especially appreciate the contributions of Jason Tomlinson, Albert Mendoza, and Peter Carrol. The wind tunnel tests were conducted at the Kristen Wind Tunnel at the University of Washington, Seattle. Several flight tests were performed in collaboration with the University of Mississippi Raspet Flight Research Laboratory on their TigerShark UAS.

Acronyms and Abbreviations

2D	two-dimensional
3D	three-dimensional
AAF	ARM Aerial Facility
AIMMS	Aircraft Integrated Meteorological Measurement System
AoA	angle of attack
AoS	angle of sideslip
ARM	Atmospheric Radiation Measurement
BFS	back-faced step
CDP	cloud droplet probe
DAQ	data acquisition
DNS	direct numerical simulation
IAS	indicated air speed
ID	internal diameter
IRGA	infrared gas analyzer
ISO	International Organization for Standardization
I2C	inter-integrated circuit
KWT	Kristen Wind Tunnel at the University of Washington
LFE	laminar flow element
MFC	mass flow controller
MOC	mobile operations center
mMSL	meters above mean sea level
NACA	National Advisory Committee for Aeronautics
OD	outside diameter
PCASP	passive cavity aerosol spectrometer probe
PCL	Particle Loss Calculator
PM	particle matter
PNNL	Pacific Northwest National Laboratory
POPS	printed optical particle spectrometer
RH	relative humidity
SGP	Southern Great Plains
SLPM	standard liters per minute
SPI	serial peripheral interface
TAS	true air speed
UART	universal asynchronous receiver/transmitter
UAS	uncrewed aerial system
UAV	uncrewed aerial vehicle
UDP	User Datagram Protocol
US EPA	United States Environmental Protection Agency
UW	University of Washington
WMO/GAW	World Meteorological Organization/Global Atmosphere Watch Program

Contents

Figures

Tables

The purpose of the inlet system is to provide a sample aerosol that is representative of ambient air, but at a controlled relative humidity, to the various aerosol analysers and samplers in the field laboratory. Humidity control is desirable because of the strong influence of relative humidity on the size of most airborne particles.

WMO/GAW Report #227

1.0 Introduction

Sampling for aerosols imposes special requirements for an inlet system that should transport the air sample to the sensors with minimal distortions to the aerosol size distribution, total concentration, and chemical composition; detailed discussions can be found elsewhere (e.g., WMO/GAW 2016 or Baumgardner et al. 2011). Sampling from a relatively fast mobile platform simplifies the design since the incoming air flow is expected from a relatively narrow directional segment; hence the inlet does not need to be omnidirectional. However, this imposes another constraint on the inlet: the actual sample separation should be made in undisturbed air − that is, the inlet tip should be far enough upstream from the platform.

Three main requirements for the inlet system are:

- Air velocity inside the inlet entrance (tip) should be the same as incoming air velocity (isokinetic sampling condition);
- Minimal particle losses inside the inlet and sample distribution system; and
- Temperature and humidity should be maintained close to the ambient or, if not possible or practical, relative humidity should be dropped below 40% (generally accepted threshold for aerosol considered to be in a "dry" state; see WMO/GAW 2016) while temperature should not exceed 40°C (to minimize volatilization of volatile and semi-volatile constituents).

Some of the requirements include contradictory conditions, e.g., minimal particle loss can be achieved by maintaining isokinetic conditions in flow splitters, electrically conductive walls (avoid electrostatic losses), preferably laminar flow (to lower diffusion and impact losses), but highest air speed to minimize residence time and, hence, sedimentation and diffusion losses.

Anisokinetic sampling leads to distortion of the aerosol size distribution and total concentration (for examples of flow patterns; see, e.g., Wilcox 1956): sub-kinetic sampling (inlet tip air speed below incoming air speed) results in overestimation of the larger-size aerosols and total concentration, while super-kinetic sampling (inlet tip air speed exceeding incoming air speed) leads to underestimation of the larger-size aerosols and total concentration. Note that isokinetic conditions have to be maintained throughout the whole aerosol sample distribution system at any sample flow separation point (e.g., a line splitter or a pickoff). Obviously, a threshold between isokinetic and anisokinetic sampling has no "first principle" definition, so it is customary to define a ±10% envelope around a strictly isokinetic state to be considered isokinetic sampling (e.g., U.S. EPA Method 5 − Particulate Matter (PM), https://www.epa.gov/emc/method-5-particulate-matter-pm).

The aerosols (natural, anthropogenic, and laboratory generated) quite often exhibit hydroscopic features – size growth at elevated relative humidity due to water uptake or vice versa, decreasing sizes as relative humidity drops. Therefore, it is desirable to measure aerosol properties at "original" (ambient)

temperature and humidity conditions or at some "standard" generally accepted state. Currently, the World Meteorological Organization Global Atmosphere Watch Program guidance (WMO/GAW 2016) recommends aerosol measurement at relative humidity (RH) levels below 40%, which allows post-processing correction of the size and radiation properties to the ambient conditions, provided aerosol humidification and hygroscopic growth factors are known.

The inlet systems for an uncrewed aircraft system (UAS) have to conform with additional requirements specific to small aerial platforms: compact, minimal weight and power consumption, fully automated or capable of functioning with minimal operator's intervention via remote control, operate in non-pressurized and not climate-controlled environment, sustain considerable vibration and broadband radio frequency interference.

Note that the inlets must be well characterized for aerosol transmission efficiency (particle loss, cut-off sizes, etc.). However, direct characterization of an airborne inlet constitutes a serious engineering problem, the solving of which usually involves multiple tests in a specialized wind tunnel and in most cases is cost prohibitive and can be non-conclusive. We have estimated the transmission efficiency for aerosol inlets per se (excluding the sample distribution sub-system) using the Particle Loss Calculator (PLC; described in von der Weiden et al. 2009; available from Max-Planck Institute for Chemistry).

The main purpose of this report is to document the design of two aerosol inlets suitable for deployment on a fixed-wing uncrewed aircraft system. The report contains sufficient details so that both designs can be customized by qualified engineers for specific sampling and/or deployment requirements.

One of the described aerosol inlets is a simple, passive apparatus suitable for an instrument with low sample flow rate (controlled by an internal pump of the instrument). The inlet is small and transformable enough to be installed in a pylon or in a main aircraft body, as a single unit or in a "distributed" fashion (allows for long flexible lines between main parts). The temperature of this small inlet is expected be close to ambient, so no humidity control is used. The other described design is for an active isokinetic inlet with a non-disturbing humidity conditioner capable of supplying considerable air flow to a suite of heterogeneous sensors (aerosol sizers, samplers, counters, gas analyzers, etc.).

All calculations of air speeds, dynamic pressures, pressure differences, air density, etc. were made for fixed relative humidity (50%) or dry air (no humidity) as it is customary in aviation; accounting for humidity effects should modify the results by few percent, but will not change the general picture.

The values and sizes are expressed in metric units except when the sizes are originally defined in the American customary units, e.g., tube sizing.

2.0 Passive Inlet for a Pylon-Mounted Sensor

The passive inlet described below was designed for a printed optical particle spectrometer (POPS; see Gao et al. 2016 and Mei et al. 2020) mounted in a custom pylon to be deployed on the ArcticShark UAS platform. The current design can easily be adopted for another sensor, mounting style, and/or platform type following our design steps and logic.

2.1 General Requirements for the Inlet

The designed inlet should have the following capabilities and features:

- Provide near-isokinetic sampling for the POPS at cruise speed of the ArcticShark (IAS≈60−68 kt)
- Provide minimal particle loss for the POPS's size range (0.1 to 3 μm)
- Passive (no moving parts, electric power for monitoring but not for operation)
- Minimal weight
- Adaptable enough to fit into a confined space or allow "distributed" arrangement of the parts
- Minimize probability of cloud droplets entering the POPS inlet line
- Provide in-flight monitoring of the inlet performance
- Simple and cost effective for manufacture and duplication.

2.2 Design Inputs, Assumptions, and Considerations for Determining Physical Dimensions

After we tried several layouts of inlet prototype, the final inlet topology was chosen as follows:

- Front cone with expansion angle small enough to avoid air flow separation from the walls (no turbulent and recirculation zones).
- Main tube long enough for the laminar flow developing in the tube and to place the inlet tip far enough off the pylon in undisturbed air flow; the main tube ID value is a compromise between minimum sample residence time (i.e., highest air speed inside the tube) and laminar flow conditions (air speed well below critical value corresponding to local Reynolds number of 2300).
- Manifold with the streamlined pickoff for POPS inlet in the 45° turn of the main line, Venturi flow meter, two side ports downstream of the Venturi for POPS sheath and exhaust flows, and second 45° turn to point the main line down. NOTE: the POPS pickoff protrudes in the main line for at least one main line ID upstream of the beginning of the first 45° turn and it is mounted above the main tube center line by 0.7 of main tube radius.
- Exhaust section: a flow-restricting element (abrupt contraction in the line) and a wedge-shaped scarf (source of vacuum for inlet operation) mounted on the bottom of the pylon on the outside surface.

This list of design parameters should be combined with a set of known parameters of the sensor and the platform (design "inputs" listed in Table 1) and certain commonsense assumptions (listed in Table 2) to provide sufficient information to calculate and justify all inlet parameters including dimensions and air speeds (listed in Table 3).

Table 1. Design inputs ("given" parameters).

Parameter	Value	Comment
Platform speed	35 m/s or 68 kt IAS	Upper range of ArcticShark cruise speed (loiter speed)
POPS nominal sample flow	3 cc/s or 0.18 SLPM	NOTE: the flow is maintained as constant *mass* flow
POPS inlet line	1/8" stainless steel (SS), nominal ID of 1.75 3 mm	NOTE: air speed in the inlet line is V_p=*1.24* m/s for nominal flow rate

Table 2. Design assumptions (commonsense considerations).

Assumptions and rationales	Affected parameter(s)	Notation	Value or range
Isokinetic inlet sampling – tip air speed equals the ambient incoming flow air speed	Incoming air speed and tip air speed	$V_\infty = V_{tip}$	35 m/s
Pickoff diameter matched to the POPS inlet line (nominal ID of 1/8" SS tube)	Pickoff ID	D_p	1.753 mm
Isokinetic pickoff sampling − air speed in the main part equals the pickoff air speed (1.24 m/s)	Main part air speed	V_m	1.24 m/s
Pickoff positioning: above the center line of main tube by 0.7 of main tube radius to be in the part of air flow where the velocity is close to the mean air velocity through the tube (parabolic velocity profile for laminar flow in tubes)	Pickoff positioning in the main tube		Above center line by 0.35 of main tube ID
Reasonable inlet orifice size to have the total inlet flow about 50 times larger than POPS inlet at ArcticShark speed and isokinetic sampling at the tip	Tip ID	D_{tip}	2.54 mm
Flow inside the cone does not separate from the walls: expansion angle below 11°; assume safe margin of 1°	Cone expansion angle	α	10°
Laminar flow in the main inlet tube	Reynolds number in the main section	Re_m	≈800 (best case) <2300 (at least)
No flow separation from the walls in turns: turn center line radius scales with line ID	Turn center line radius scaling factor		2 to 3
Venturi flow meter with modest contraction ratio: tradeoff between sensitivity (the higher the better) and flow disturbance/resistance (the smaller the better)	Contraction ratio	c_r	About 2
Laminar flow in the Venturi contraction	Reynolds number in the Venturi contraction	Re_c	≤2300
Reasonable atmospheric conditions and ambient air parameters (constant) No heat exchange; neglect ram heating, expansion cooling, etc.	Air temperature Air pressure Relative humidity Air density Air viscosity (kinematic)	T P RH ρ v	20°C 1000 mB 50% 1.1835 kg/m^3 1.506e-5 m^2/s

Assumptions and rationales	Affected parameter(s)	Notation	Value or range
Two side ports after the Venturi flow meter to supply POPS sheath flow and allow dumping of the exhaust flow at the same pressure as POPS inlet in order not to strain the POPS pump; exact position of the ports is not important as long as they are downstream of the pickoff	Side port diameter		1.753 mm

Table 3. Calculated parameters and dimensions.

Parameter	Notation	Rationale and formula	Value
Inlet flow rate	F_{in}	Estimated tip flow for isokinetic sampling at ambient air speed (35 m/s) through tip orifice of 2.54 mm $$F_{in} = \pi D_{tip}^2 V_{tip}/4$$	10.64 LPM
Main diameter	D_m	Isokinetic sampling with pickoff in the main part: main part air speed should be close to the pickoff air speed (1.24 m/s) maintaining tip flow rate $$D_m = 2\sqrt{F_{in}/(\pi V_p)}$$	13.49 mm
Cone length	L_c	The cone section should provide smooth expansion from the tip ID to the main part ID with chosen expansion angle α $$L_c = (D_m - D_{tip})/(2tan(\alpha/2))$$	62.7 mm
Main part length	L_m	Main part should provide reasonable distance for laminar flow stabilization/formation and gravitational settling of largest cloud droplets: $$L_m = 10D_m$$	135 mm
Main part Reynolds number	Re_m	Laminar flow condition (Re≤2300) $$Re_m = \frac{V_m D_m}{\nu}$$	1114
Venturi contraction Reynolds number	Re_c	Laminar flow condition (Re≤2300) $$Re_c = \frac{V_c D_c}{\nu} = \frac{V_m D_m c_r}{\nu}$$	2228
POPS pickoff Reynolds number	Re_p	Laminar flow condition $$Re_p = \frac{V_m D_p}{\nu}$$	145
45° turn center line radius	R_t	No flow separation from the walls in the turn – minimal radius (Idelchik, 2007): $$R_t = 2D_m$$	27 mm

Parameter	Notation	Rationale and formula	Value
Venturi flow meter		Following recommendations in ISO-5167-4:	
	c_r	Contraction ratio	2
	D_{thr}	Throat ID $D_{thr} = D_m/c_r$	6.75 mm
		Length of straight section upstream contraction	50.8 mm
		Contraction angle	10.5°
		Contraction length	14.48 mm
		Throat length	6.75 mm
		Diffusor angle	4°
		Diffusor length	28.96 mm
		Length of straight section downstream of diffusor	38.1 mm
Flow restriction diameter		Estimated ID to balance scarf suction (available vacuum) with total flow resistance of the inlet; see Sect.2.3	3.42 mm

The final inlet prototype was manufactured in three main pieces: (1) inlet tip (front cone and main tube) made of aluminum (Figure 1); (2) conductive 3D-printed manifold combined with Venturi tube and equipped with stainless-steel tube insert for POPS sample pickoff and side taps for Venturi pressure difference sensor and POPS housekeeping flows (Figure 1); (3) 3D-printed scarf section mounted on the bottom side of the pylon with hole and O-ring to accommodate the bottom end of the manifold.

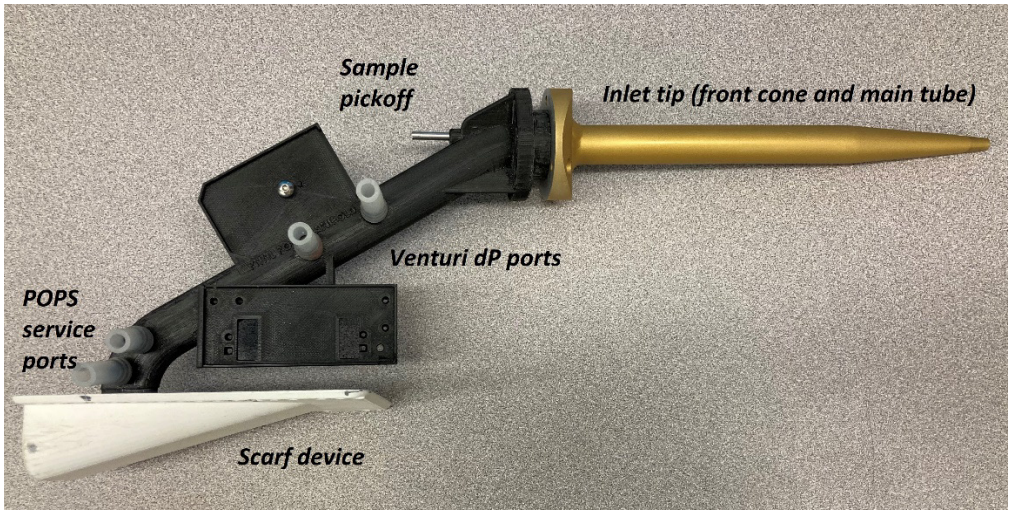

Figure 1. Main parts of the inlet prototype: inlet tip (front cone and main tube, golden), 3D-printed manifold with Venturi tube (black), and scarf device (white). NOTE: the sample pickoff is mounted above the center line of the main tube and extends into the tip for about 10 mm beyond the tip/manifold junction.

We expect the flow in the main tube to be laminar near the POPS sample pickoff, so the pickoff must be shifted up from the axis of the main tube by 0.7 of the main tube's radius to the position where local air speed equals nominal mean air speed in the main tube (well-known feature of a parabolic velocity profile of laminar flow in a pipe; details on laminar flow in pipes can be found in any fluid dynamics textbook, e.g., Landau and Lifshitz 1959.)

2.3 Air Speed at the Inlet Tip as a Function of Platform Speed

The air flow through our passive inlet is determined by the balance between vacuum ΔP_{vac} generated at the back end of the inlet (scarf suction) and flow resistance of the inlet (or total pressure drop ΔP_{tot} over the inlet):

$$\Delta P_{tot} \approx \Delta P_{vac}$$
$$\Delta P_{tot} = \Delta P_{inlet} - \Delta P_{tip}$$
$$\Delta P_{tip} = sgn(V_\infty - V_{tip}) \cdot \rho \cdot \left(V_\infty - V_{tip}\right)^2/2,$$

where the total inlet pressure drop is split into two parts: ΔP_{inlet} is the pressure drop over the inlet per se, which depends only on inlet geometry and flowrate, while the other part, pressure drop at the tip ΔP_{tip}, depends on difference between the incoming flow speed V_∞ (platform speed) and speed of air in the tip V_{tip}. In the super-kinetic regime ($V_\infty < V_{tip}$), the tip pressure drop increases the total inlet pressure drop by a part necessary to accelerate the inlet flow to the speed of V_{tip}, while in the case of the under-kinetic regime ($V_\infty > V_{tip}$), this part of ram pressure should be considered as addition to the scarf vacuum. The signum function $sgn(V_\infty - V_{tip})$ depicts this sign change in the equation above. Obviously, in the perfectly isokinetic case, the tip pressure drop disappears.

Scarf suction vacuum is generated by a turbulent area behind a back-faced step (BFS) where, if put in a very simplistic way, the local air speeds in vortices are much higher, and consequently, the local pressure is lower. Flow characteristics behind the BFS have been purposefully investigated (e.g., see Chen et al. 2018); however, pressure distributions on the back face are usually not reported in an explicit way.

A pressure drop behind a wedge-shaped scarf can be estimated using experimental results by Nash et al. (1966). They performed a set of wind tunnel experiments in which they estimated, among other things, the pressure coefficient $C_p = \frac{P_l - P_\infty}{\rho V_\infty^2/2}$ behind the back-faced ledge. All experiments were made for Mach numbers from 0.2 and up to 1.05 and in approximation of two-dimensional objects: width (horizontal, cross-stream) was much larger than height (vertical, cross-stream) for all models. They presented a plot of $C_p(M)$ as a function of Mach number M from which we estimated $C_p(0.2) \approx -0.25$; this plot suggests an upward trend in C_p value as Mach numbers decrease below 0.4 toward 0.2.

Barri et al (2010) reported similar value for $C_p \approx -0.28$ in a direct numerical simulation (DNS) study of developed turbulent flow over a back-facing step.

Our wedge-shaped scarf with an expansion angle of 10° differs in several ways from the models and conditions of the Nash et al. (1966) experiments: The Mach number at the ArcticShark's nominal cruise speed is about 0.1; our scarf is definitely not a 2D object: its sizes in all dimensions are of the same order; it is placed on the bottom surface of the pylon (a relatively narrow surface – not an infinitely wide plate) not far from the front edge of the surface. We should expect a somewhat higher value of the C_p due to three-dimensional effects and a lower Mach number; however, as a conservative estimate we have accepted the smallest scarf pressure drop of $\Delta P_{vac} = 0.25 \cdot (\rho V_\infty^2)/2$ in our initial round of calculations. For the nominal cruise speed of the ArcticShark, the scarf suction ΔP_{vac} is about 181 Pa.

A pressure drop over the whole inlet could be estimated as superposition of pressure drops over each inlet element; in the first order approximation the interference between the elements due to their close proximity could be neglected. Individual pressure drops for each element were estimated using a hydraulic resistance handbook (Idelchick 2007). Note that Idelchick (2007) is an engineering handbook: it is based mostly on empirical estimates and geared toward industrial applications with much larger physical dimensions, flow rates, and Reynolds numbers.

Generally, the flow resistance of an element is expressed via dynamic pressure after the element and coefficient of fluid resistance (pressure loss coefficient) $\Delta P_{ov} = \zeta_{ov}\,\rho V^2/2$, where overall resistance coefficient $\zeta_{ov} = \zeta_{loc} + \zeta_{fr}$is usually split in two parts – coefficient of local fluid resistance ζ_{loc} and coefficient of friction resistance ζ_{fr}. The friction part is expressed as a product of friction coefficient λ (usually reverse proportional to local Reynolds number *Re* with dependence on wall roughness) and some function of the element shape (for simple shapes – nondimensional length); note that pressure loss due to friction is an implicit function of air speed behind the object. The coefficient of local fluid resistance is usually some empirical function of the element shape; note that pressure loss due to local resistance is proportional to the square of the air speed behind the object.

The coefficients of fluid resistance for all elements of the inlet are described in Table 4, which can be used to estimate total pressure drop over the inlet as a function of tip air speed. We adopted a conservative approach for the evaluation of the inlet pressure balance – when in doubt, the highest flow resistance and lowest available vacuum were used. The result should correspond to the worst-case scenario and the real inlet should perform better than our rough estimate.

Table 4. Fluid resistance coefficients for main elements of the inlet.

Element	Equations for coefficients	Comments, diagram, page, and/or formula # in Idelchik (2007)
Front cone	$\lambda_{in} = 0.3164/Re_{tip}^{0.25}$ $\lambda_{out} = 64/Re_m$ $\lambda = \max(\lambda_{in} + \lambda_{out}) \Rightarrow \lambda = \lambda_{out}$ $\zeta_{fr} = \frac{\lambda}{8sin(\alpha/2)}\left(1 - \frac{1}{(D_{tip}/D_m)^4}\right)$ $\zeta_{cone} = 3.2tan(\alpha/2)^{1.25}\left(1 - \frac{1}{(D_{tip}/D_m)^4}\right)^2$	For *Re>4000*, diagram 2-1, page 85 For *Re<2000*, diagram 2-1, page 85 To be "conservative" (5-6) page 192 (5-5) page 191
Main tube	$\lambda_m = 64/Re_m$ $\zeta_m = \lambda_m \frac{L_m}{D_m}$	diagram 2-1, page 85

Element	Equations for coefficients	Comments, diagram, page, and/or formula # in Idelchik (2007)
Pickoff	$L_p = D_m + \sqrt{R_t^2 - (R_t - D_m/4)^2}$ $\zeta_{fr} = \lambda_m \frac{L_p}{D_m}$ $\xi_p = 1.2 \frac{(D_p/D_m)^2}{\left(1 - 0.5(D_p/D_m)^2\right)^3} 0.5^{1/3}$	Length of the pickoff part exposed to the main flow Fluid resistance due to friction on outside surface of the pickoff diagram 10-9, page 490
45° turn	$L_t = \pi R_t/4$ $\zeta_{fr} = \lambda_m \frac{L_t}{D_m}$ $\zeta_t = 0.9 \sin 45° \frac{0.21}{\sqrt{R_t/D_m}}$	L_t is length of the turn along the center line (6-1) page 260
Venturi: converging-throat-diverging section	$\zeta_v = k_1 k_2 \zeta_1 + \Delta\zeta$ $k_1 = 1.0;\ \ k_2 = 1.01$ $\zeta_1 = 0.3$ $\Delta\zeta = 0$	Diagram 5-25 and 5-2 Contraction ratio 2, total angle 21°; throat length to diameter ratio close to 1, and low Re<2e5
Exhaust: flow restriction	$D_m \rightarrow D_{rest}$ $\zeta_{rest} = \gamma$	For change from main diameter to flow restriction element ID diagram 4-10, page 166 γ – linear approximation of table values
Exhaust stab	$\lambda_{rest} = 64/Re_{rest}$ $\zeta_{rest} = \lambda_f \frac{L_{rest}}{D_{rest}}$	Diagram 2-1, page 85
Transition from D_{rest} to scarf		No information

The front cone friction part is conservatively estimated by "laminar" flow approximation. Air flow in the tip is not fully developed: it begins as a "plug" flow, but with high enough local *Re* value to suggest transition to turbulent flow. However, cone expansion lowers local *Re* below laminar threshold in a short distance or a few milliseconds of travel time (about 30mm and 5ms for isokinetic conditions at nominal cruise speed). Most probably, the flow in the front cone does not transition to full turbulent state, but rather evolves into developed laminar flow in the main tube of the inlet with local *Re* value well below turbulent threshold (local *Re=1114* for isokinetic conditions at nominal cruise speed).

A flow restriction element, in the exhaust section, is added to fine tune the total pressure drop over the inlet to balance the scarf vacuum when the tip air speed equals the platform speed (isokinetic sampling). Unfortunately, we were unable to find an adequate expression to estimate the pressure drop in the exhaust/scarf section: transition from cylindric channel to expanding rectangular wedge oriented at a right angle to the channel; we expect it to be in the order of a few Pascals, which could be included in the flow restriction pressure drop estimate.

An example of flow balance equation parts plotted as a function of tip air speed balanced on nominal cruise speed of the ArcticShark is presented in Figure 2. The flow restriction ID has been selected to

achieve pressure balance at isokinetic regime. A line corresponding to inlet pressure drop ΔP_{inlet} without flow restriction element is plotted to show that the major inlet flow resistance comes from the flow restriction element introduced to achieve pressure balance near an isokinetic state. The available vacuum (at least 145 Pa, magenta line) exceeds the inlet pressure drop (no restriction, from 1 to 2 Pa, cyan line) by two orders of magnitude, even in our conservative-style estimates. For practical purposes, the inlet flow resistance could be approximated by just resistance of the flow restriction element. This conclusion is somewhat paradoxical – the analysis showed that most of the analysis was not necessary, but to get to the conclusion we had to perform the analysis.

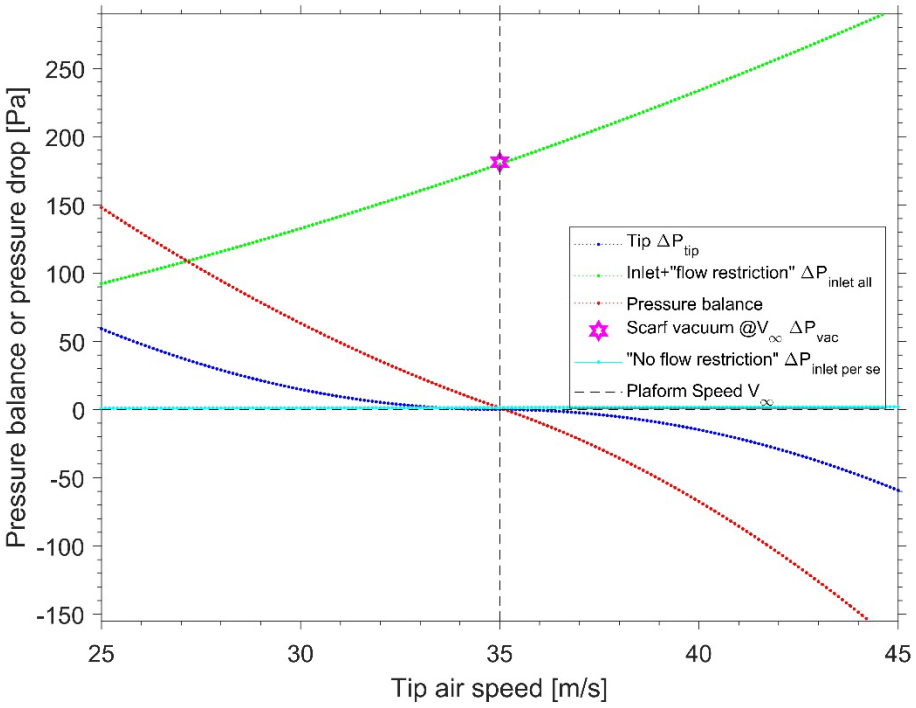

Figure 2. Various part of the inlet pressure balance equation. Vertical dashed line shows platform speed (V_∞=35 m/s). The scarf pressure drop coefficient used is C_p=0.25; restriction ID, necessary to balance pressures, is 3.42 mm.

The tip air speed estimates as a function of the platform speed (Figure 3) show the self-regulating nature of the inlet over a wide range of speeds. Lines corresponding to different flow restriction element IDs converge up to some ultimate line corresponding to the inlet with no flow restriction; however, they do not reach the area of experimental Kirsten Wind Tunnel (KWT) data (see Section 2.5.2 for details of the wind tunnel tests). The main reason for this discrepancy is our conservative approach in calculations, especially the use of the lowest estimate of the available vacuum.

Our "handbook" estimate is too rough for quantitative results, obviously, but it is good enough to capture the main features and to provide initial estimates and directions for final adjustment. Note that pressure balance and corresponding tip air speed are very sensitive to flow restriction element size near to the isokinetic regime and are much less sensitive approaching the super-kinetic extreme. The estimate of the available vacuum is the source of the main uncertainty in our analysis: a few percent change in C_p value brings a dramatic change in available vacuum ΔP_{vac} and shifts the pressure balance (see Figure 4).

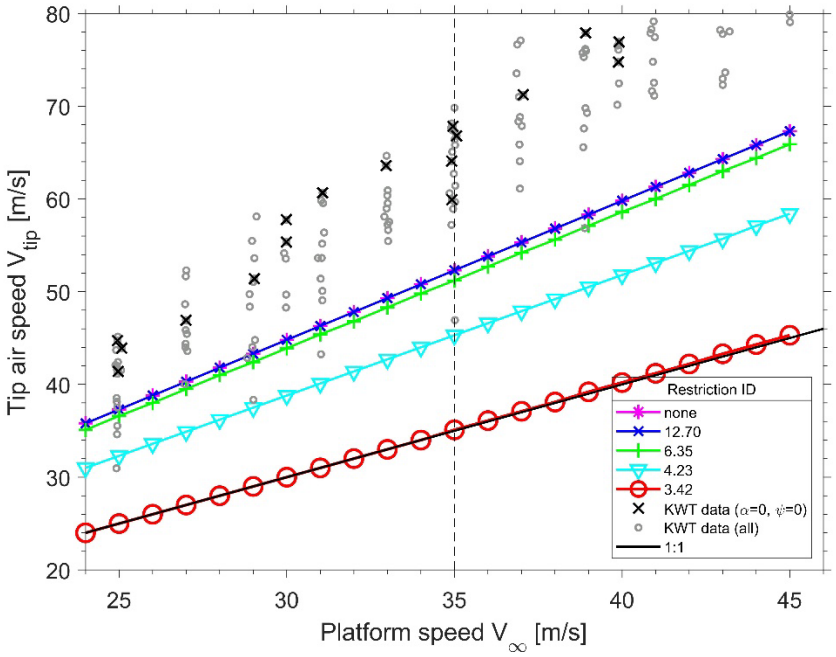

Figure 3. Theoretical evaluation of the inlet tip air speed as a function of the platform speed for several values of flow restriction element IDs. Black and grey markers show Kirsten Wind Tunnel experimental results; black Xs depict runs with streamlined inlet orientation (zero value for angles of attack α and sideslip ψ); grey circles show all other runs.

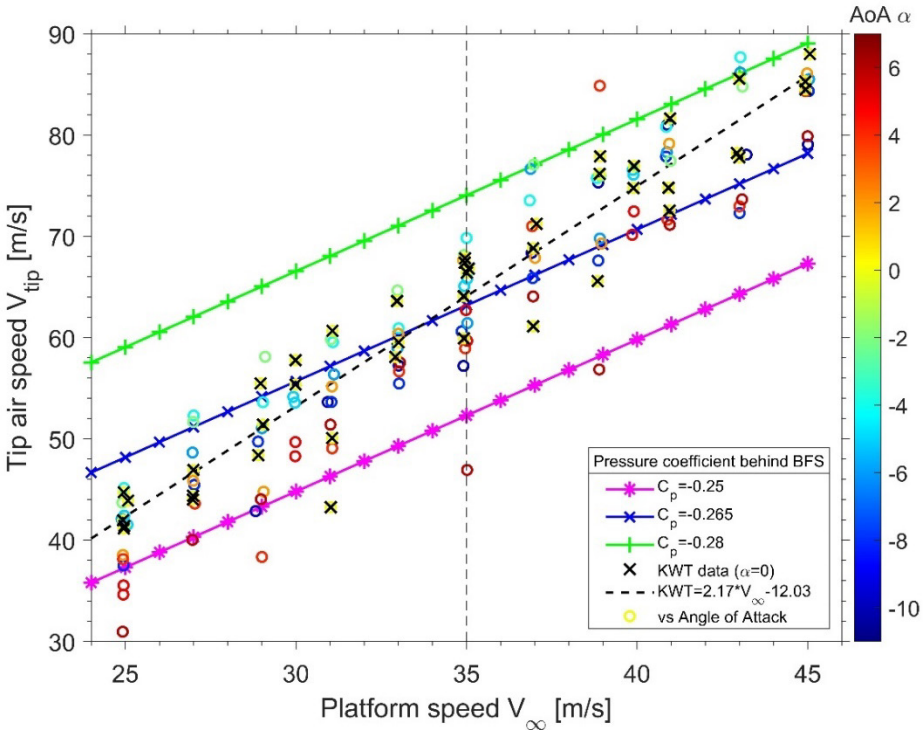

Figure 4. Inlet tip air speed estimates for "no restriction" inlet configuration and several values of available vacuum (pressure coefficient C_p) to mimic conditions and results of tests in the Kirsten Wind Tunnel (lines). Experimental KWT data are shown with black Xs (α=0°) or color-coded circles according to the angle of attack α.

The inlet prototype used in the KWT tests had no flow restriction element installed, so to mimic KWT test conditions we calculated versions of inlet tip speed with no flow restrictor for three different C_p values: -0.25 as per Nash et al. (1966), -0.28 as per Barri et al. (2010), and -0.265 – an arbitrary value in between the other two. Experimental points are mostly bracketed by our evaluation lines; however, a linear regression line through the experimental data calculated for points with zero angle of attack (AoA) has a steeper slope than the slopes of our estimates (2.17 as opposed to 1.5). Our estimate does not account for many details of a real-world experiment – for example, a pylon is a substantial structure that affects incoming flow, so the flow in the vicinity of the scarf element is decelerated with a developing boundary layer, the thickness of which, and other properties, strongly depend on pylon geometry, angles of attack and sideslip, local Mach number, and turbulence intensity of the incoming flow. Scarf efficiency depends on air flow structure around it, especially air speed, boundary-layer thickness, and boundary-layer state (laminar versus turbulent). There is no clear-cut dependence of experimental points spread with angle of attack (color-coded circles in Figure 4); however, some general tendency of high AoA points to be below the regression line is perceptible.

2.4 Aerosol Collection Efficiency of the Inlet

The collection efficiency of the inlet (inlet tip and POPS pickoff included in the calculations) was estimated using the Particle Loss Calculator for nominal platform speed (35 m/s for the ArcticShark) and aerosol density of $\rho_p = 1.7\ g/cm^3$ (a common value for ambient, organic-dominated aerosols). Figure 5 shows efficiency curves for several cases of sampling conditions deviating from an isokinetic regime. Isokinetic collection efficiency is above 95% for particles in the range of 12 nm to 3.6 µm – much wider than the POPS sampling range of 140 nm to 3.0 µm; lower and upper 50% cutoff sizes are 1.7 nm and 12.1 µm correspondingly.

The collection efficiency in the POPS size range remains within ±5% of ideal for moderate under-kinetic conditions (up to approximately 7 m/s difference in speeds). However, this is not the case for super-kinetic regimes. Note that when the tip is out of the isokinetic regime, the POPS pickoff is also not isokinetic, but the opposite – e.g., a super-kinetic tip provides higher flow in the inlet, which makes pickoff conditions under-kinetic.

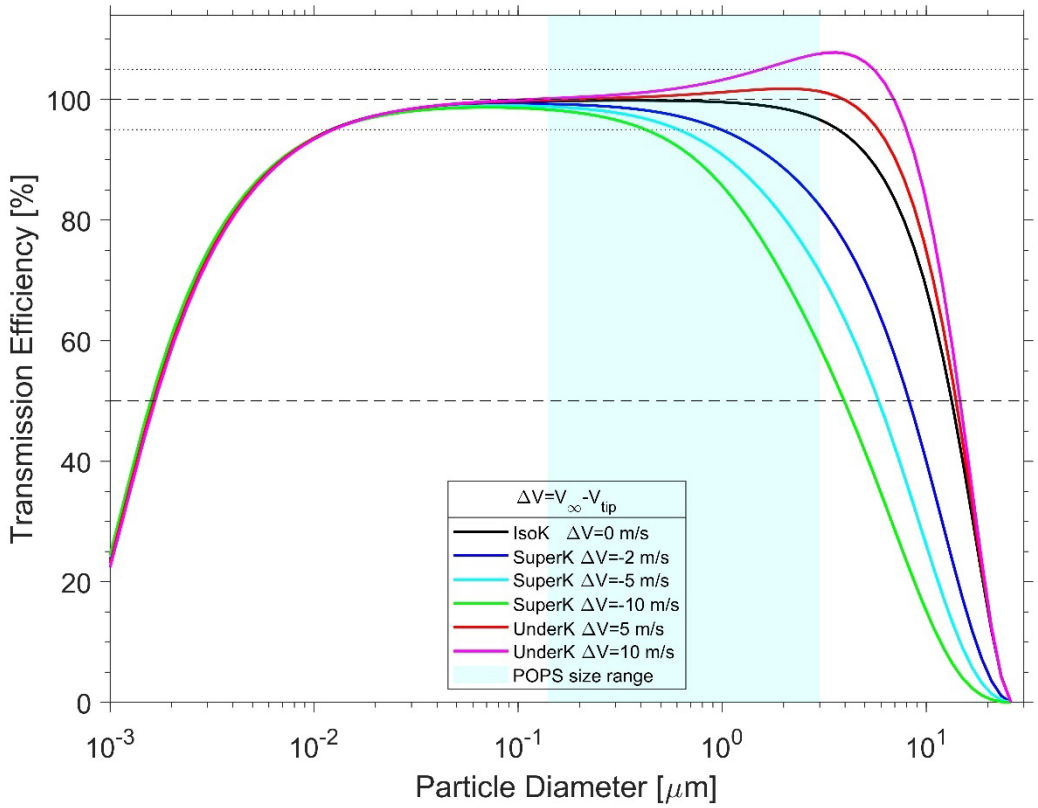

Figure 5. Aerosol collection efficiency of the passive inlet estimated with Particle Loss Calculator (von der Weiden et al. 2009). Shaded area corresponds to size range of the POPS; dashed lines show 50% and 100% efficiency levels; dotted lines mark ±5% corridor around 100%. Aerosol density was assumed to be ρ_p=1.7 g/cm^3.

The transmission efficiency curve depends on the aerosol density ρ_p: the upper cut size at a certain level (e.g., 95%) shifts up for lower ρ_p values and down for higher densities, which could be approximated by $D_1 = D_2\sqrt{\rho_2/\rho_1}$ for not too wide of a density range and the aerosol shapes close to spherical. Curves for several atmospherically relevant densities and two extremes are shown in Figure 6. Atmospherically relevant aerosol densities are for water or ice (1.0 g/cm^3), organic-dominated ambient aerosols (1.7 g/cm^3), and generic mineral dust (2.65 g/cm^3; Mahowald et al. 2014, Kesavan and Doherty 2000). Exotic extremes are fractal soot (fullerene soot or Aquadag, 0.4 g/cm^3 for near-micron-sized particles; Gysel 2011) and hematite (5.3 g/cm^3; Balkanski et al. 2007). An additional line for dust aerosols and under-kinetic sampling ($\Delta V=V_\infty-V_{tip}=5$ *m/s*) shows the advantage of an under-kinetic regime: collection efficiency remains within ±2% of an ideal 100% for the POPS size range and for an atmospherically relevant aerosol density range (from water to mineral dust).

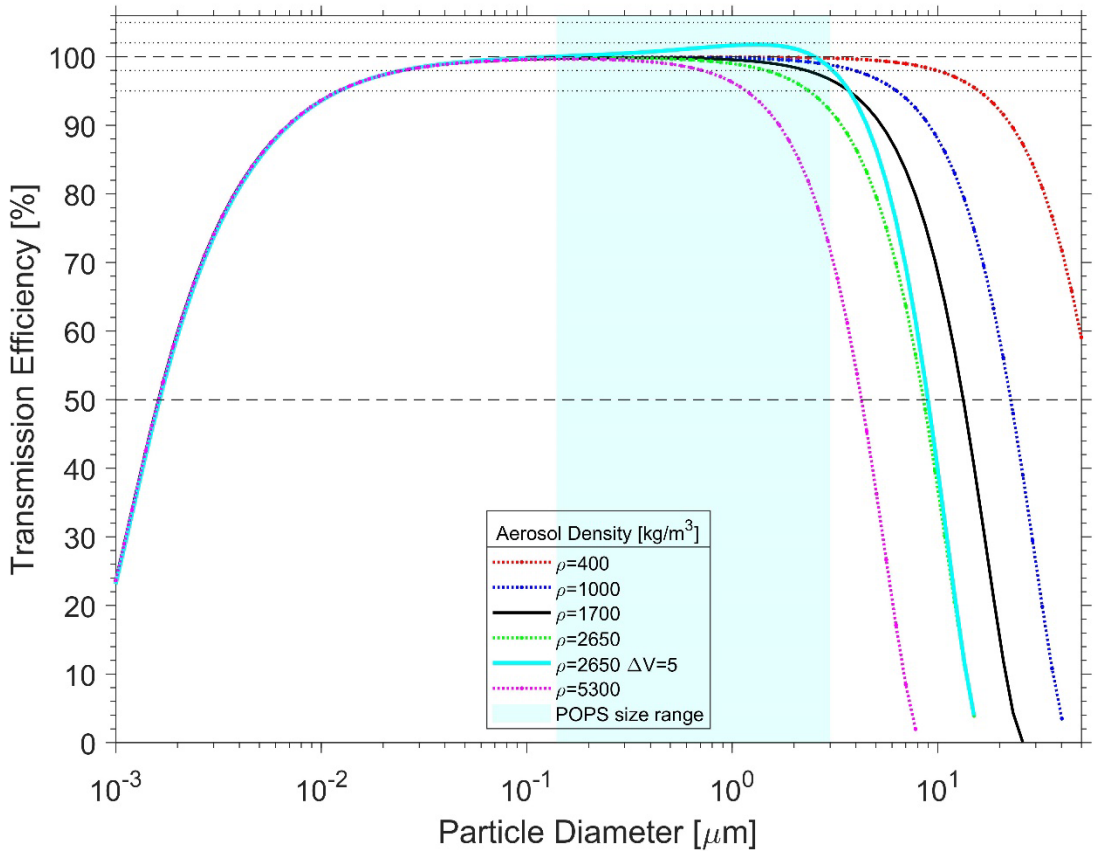

Figure 6. Aerosol collection efficiency of the passive inlet estimated with Particle Loss Calculator (von der Weiden et al. 2009) for isokinetic sampling of the aerosols with different densities: fractal soot (0.4 g/cm^3), ice/water (1 g/cm^3), organics-dominated ambient aerosol (1.7 g/cm^3), generic mineral dust (2.65 g/cm^3), and hematite (5.4 g/cm^3). The additional line for dust aerosol shows a slightly under-kinetic sampling case (ΔV=5 m/s). Shaded area corresponds to the size range of the POPS; dashed lines show 50% and 100% efficiency levels; dotted lines mark ±2% and ±5% corridors around 100%.

From Figures 5 and 6, it follows that in a final adjustment of the inlet flow (via size of flow restriction element) it might be beneficial to aim at a slight sub-kinetic regime, especially if the measured aerosols are expected to have higher density (mineral dust, volcanic ash, sea salt, metals or metal oxides, etc.). Let us keep in mind that for this passive auto-setting inlet the design sampling regime at the inlet tip (isokinetic or other) is determined by the flow restrictor element, and the regime is independent of platform speed over a wide range.

2.5 Car, Kristen Wind Tunnel, and Flight Tests

Inlet prototypes were tested in three ways: mounted on a car at highway speed, in a wind tunnel, and on a UAS in flight.

2.5.1 Car Tests

The main goal of car tests performed in June-July 2018 was “proof of a concept” as a preparation for more sophisticated tests in the Kristen Wind Tunnel. We aimed to evaluate performance of an inlet prototype and estimate efficiency of scarf “devices” as a function of their size.

A simplified inlet prototype was installed into a mockup pylon and the pylon was mounted on the roof of a pickup truck (see Figure 7). The prototype for the car test was a simplified version of the inlet assembled mostly from parts left from other projects. Only the most critical parts were specially 3D printed: two scarf devices and a “one-piece” manifold with inlet tip, main tube, and 45° turn.

Figure 7. The POPS inlet prototype mounted in the mockup pylon on the cabin roof rack of a pickup truck. AIMMS-30 was mounted side by side with the inlets about 40 cm apart. NOTE: both pylon and AIMMS-30 were mounted upside down; normally, they hang down below a UAS wing.

Two scarf devices were used. Both devices were wedge shaped, with 10° angle and rectangular cross-section with rounded corners of the same width, but of different length: 25.4 mm and 12.7 mm, so the back-end cross-sections were 50.8x4.5 mm and 50.8x2.2 mm correspondingly. The scarfs were 3D printed with small stubs to connect to the rest of the inlet via a short piece of silicon conductive tubing (0.5”=12.7 mm nominal size). The ID of the stubs was about 6 mm, so the stubs worked as an effective flow restriction element. The scarf devices were alternatively mounted on the pylon so that each was used several times throughout the tests.

Flow rate through the inlet was measured with a Venturi tube connected between the inlet manifold and the scarf and mounted inside the mockup pylon. The Venturi tube was paired with a differential pressure sensor AMS5915-0005-D-B (±5 mB; Analog Microelectronics GmbH). This flow meter was calibrated in the laboratory using a Total Sky Imager (TSI) flow meter (model 4100), Alicat mass flow controller (MFC), and Dwyne differential pressure sensor (see calibration plot in Figure 8). NOTE: the used Venturi tube was a "left over" from other project with slightly smaller sizes than in our design. A calibration coefficient and zero offset for a specific AMS5915 sensor and Venturi tube were determined, so the flow through the inlet could be estimated for car test conditions as mass flow in SLPM via $F_{in} = 9.58\sqrt{(\Delta P - 0.070)}$, where Venturi differential pressure ΔP was in Pa. Inlet tip air speed V_{tip} was calculated from the inlet flow F_{in}, measured by the Venturi flow meter, and nominal tip cross-section area $S_{tip}=\pi D_{tip}^2/4$ as $V_{tip}=F_{in}/S_{tip}$ (coefficient to convert flow from LPM to m^3/s is omitted).

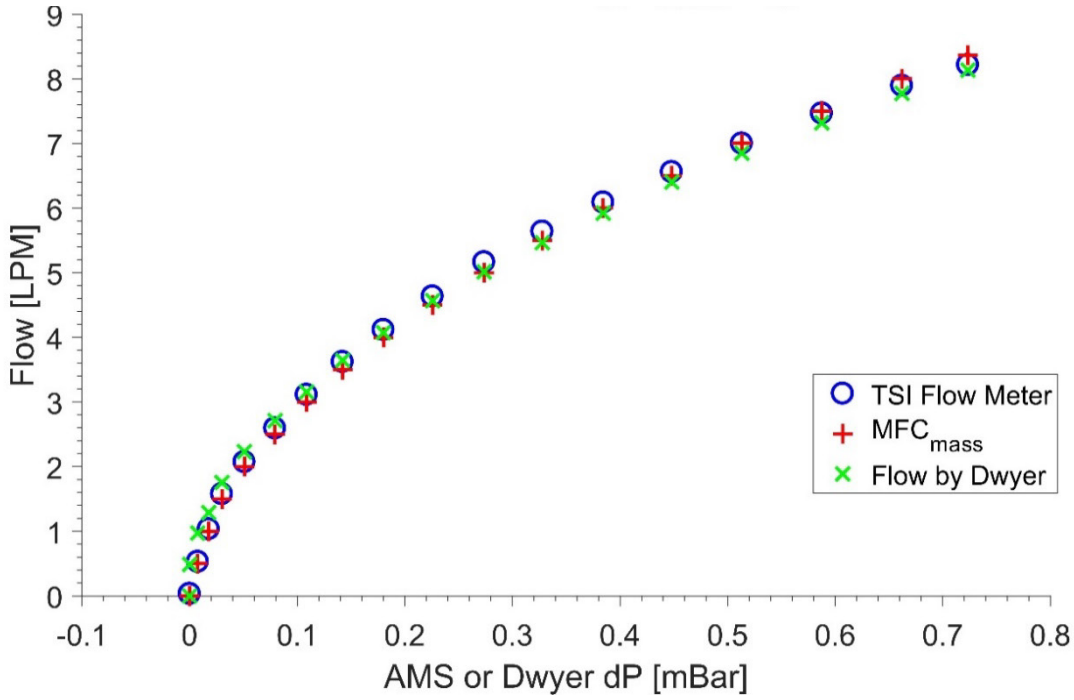

Figure 8. Calibration plot for Venturi tube. NOTE: pressure differential zero offset applied to AMS5915 data was for a specific AMS5915-00005 sensor.

An Aircraft Integrated Meteorological Measurement System (AIMMS-30) mounted side by side with the inlet was used to measure true air speed (TAS, or ambient air speed). Both mockup pylon and AIMMS-30 were mounted upside down with respect to their normal mounting on a UAS. The AIMMS-30 is capable of measuring 3D winds, but due to the upside-down mounting all wind vector components were garbled, so we used only TAS channel data. As a real-time display and a backup source of platform speed (proxy for incoming air speed), two GPS instruments were used: a Garmin GPS navigator (model Nuvi 1256) and an I-got-U GPS tracker.

The pickup truck was driven multiple times on a 4-mile (6.4 km) stretch of Interstate I-82 near Pacific Northwest National Laboratory (PNNL) in both directions with a "target" speed of 31 m/s (=70 mph, the local legal speed limit). The "target" speed of the car test falls slightly short of the "target" speed of the ArcticShark (35 m/s); however, since the main goal of the test was a proof of concept, it should suffice.

The self-adjusting behavior of the inlet over a wide range of incoming air speed is illustrated by Figure 9: scatter plot of inlet tip air speed versus ambient air speed (TAS, measured by AIMMS-30). The blue line shows an estimate of tip air speed calculated from inlet flow resistance coefficient $\zeta_{inl} = \frac{\Delta P_{inl}}{\rho V^2/2} \approx 0.303$ and expected available vacuum $\Delta P_{vac} = 0.25 \cdot (\rho V_\infty^2)/2$. The inlet flow resistance coefficient was directly measured in the laboratory: $\zeta_{inl} = \frac{\Delta P_{tot} - \rho V^2/2}{\rho V^2/2}$, where total pressure drop over the inlet ΔP_{tot} was measured as a function of tip air speed V and corrected for pressure drop $\Delta P_{acc} = \frac{\rho V^2}{2}$ necessary to accelerate the air flow from stagnation to the tip air speed.

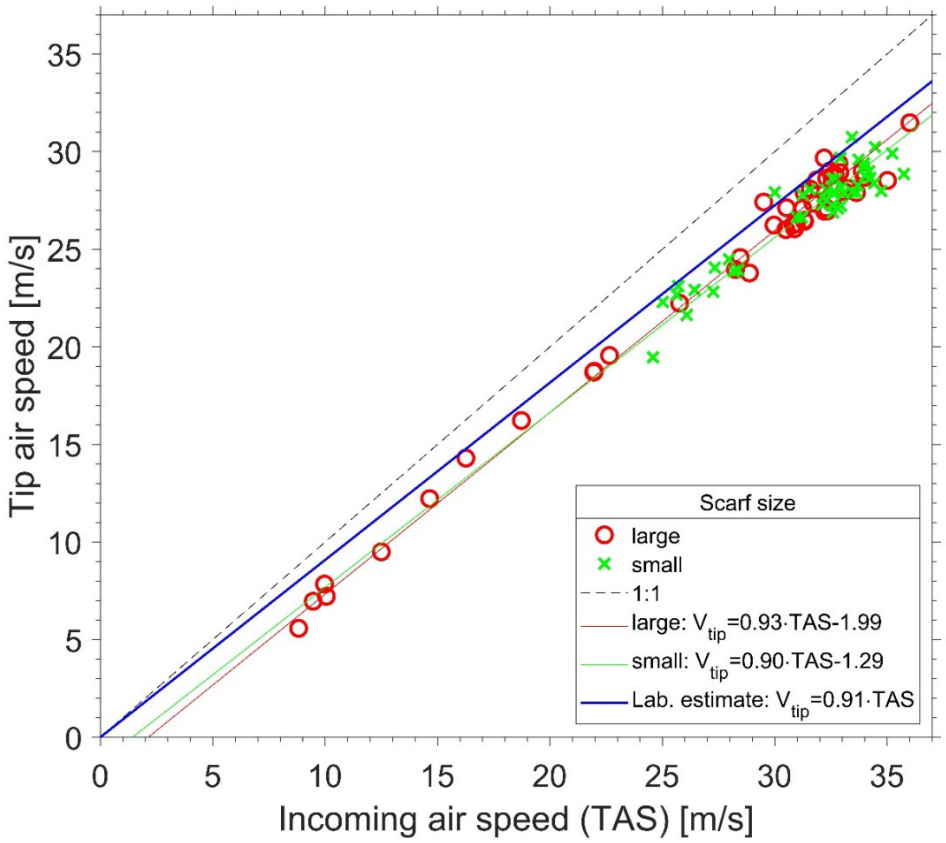

Figure 9. Calculated tip air speed versus measured incoming air speed (TAS by AIMMS-30) for car tests. Blue line depicts another estimate of the tip air speed calculated using inlet pressure resistance directly measured in the laboratory.

No difference in inlet performance was noticed between the two scarf elements used in the tests – a somewhat counter-intuitive result. It seems that a scarf with larger exhaust area should provide more suction. However, at first approximation, pressure drop at the back face of the scarf (the driving force for the inlet flow) does not depend on scarf area, but on incoming air speed only, providing that the back area is big enough and constitutes no additional flow resistance.

We note that the flow around the inlet tip was far from perfect: it was neither uniform nor aligned with the tip axis. The flow pattern around the pickup truck is not known; the flow above the cabin was most

probably not horizontal. Unknown wind and vortices from the other cars, trucks, and trailers contributed to the flow uncertainty. The pickup truck could not sustain the "target" speed at all times due to traffic; subsequently platform accelerations and decelerations added to the data spread.

Overall, Figure 9 shows a consistent picture for both scarf sizes and laboratory estimate.

The inlet was in a sub-kinetic regime with tip speed about 10% below the TAS and a perfect linear relation between them over the whole range of air speeds tested. The car tests successfully demonstrated the feasibility of the concept and supported the results of our theoretical estimates.

2.5.2 Kristen Wind Tunnel Tests

A wind tunnel test was conducted in the Kristen Wind Tunnel at the University of Washington, Seattle in September of 2018. The main objectives of the test were:

- Test the inlet and the pylon in fully controlled environments
- Assess impact of inlet misalignment with incoming air flow (angles of attack and sideslip) on inlet performance
- Check POPS operation in conditions close to real flight in terms of sample flow disturbance, pump load, etc.
- Check scarf devices performance (three different sizes)
- Visualize the flow structure around the pylon to check for turbulent zones and other flow disruptions, and if the inlet tip is long enough to bring the sampling point out of the area of flow disturbance.

No special test aerosol was generated – "naturally" occurring background aerosol in the Wind Tunnel was used.

The pylon with the POPS installed inside was mounted on the main turntable in upside down position (Figure 10). All attitude angles are reported with respect to this mounting. A passive cavity aerosol spectrometer probe (PCASP; Liu et al. 1992) was used as a reference aerosol spectrometer sensor; it was mounted on a separate fixed arm about 0.8 m off the POPS pylon. The PCASP is a "mature" sensor that has been used in airborne aerosol research since the mid-1980s: it is well known and well characterized. The PCASP was not intended to be a reference to compare POPS with, but rather a monitor that shows the status of the sampled aerosol – time variation in size-resolved concentration to distinguish changes in the POPS signal due to inlet performance/orientation from changes in background aerosol loading and size distribution shape.

Figure 10. The pylon with POPS and inlet mounted on the main turntable inside the Kristen Wind Tunnel. The PCASP is mounted on a separate fixed arm.

We performed a set of test runs covering a matrix of air velocities and attitude angles (attack and sideslip angle) to measure (a) flow through the inlet and (b) aerosol size distributions. The air speed in the tunnel was varied from 25 to 45 m/s in 2 m/s increments; angle of attack was changed between -10° and +6° in 2 increments; angle of sideslip was limited to three positions: -5°, 0°, and +5°. Most of the runs were made with a "normal"-sized scarf; two other sizes (one-half and one-quarter length) were used to check if scarf size affects inlet efficiency at different angles of attack. Data accumulation time in each position was between 15 seconds and 3 minutes. The range of air speeds covered in the test was much wider than the anticipated cruise speed range of possible platforms (ArcticShark – up to 35 m/s, TigerShark – about 28 m/s). Please note that due to time constraints not all permutations of wind speeds and attitude angles were covered.

The inlet tip air speed was calculated from inlet flow measured by Venturi tube similar to the car tests (see Sec. 2.5.1); the results of comparison of the tip air speed with the incoming air speed have been partially discussed in Sec. 2.5.1.

The flow through the inlet was not limited by a flow-restricting element and the inlet was run "at full capacity", so the tip air speed twice fold exceeded ambient speed (see Figures 3, 4, and 11). For cases when the inlet was aligned with the incoming flow (angle of attack [AoA] and angle of sideslip [AoS] are 0°; 20 runs) the correlation coefficient between the inlet tip air speed and incoming air speed is 0.987; for all cases (any AoA and AoS; 146 runs) the correlation drops down to 0.947. Dots in Figure 11 are color coded with angle of attack; "reddish" dots, corresponding to extremes of AoA, tend to congregate at the bottom of the "band".

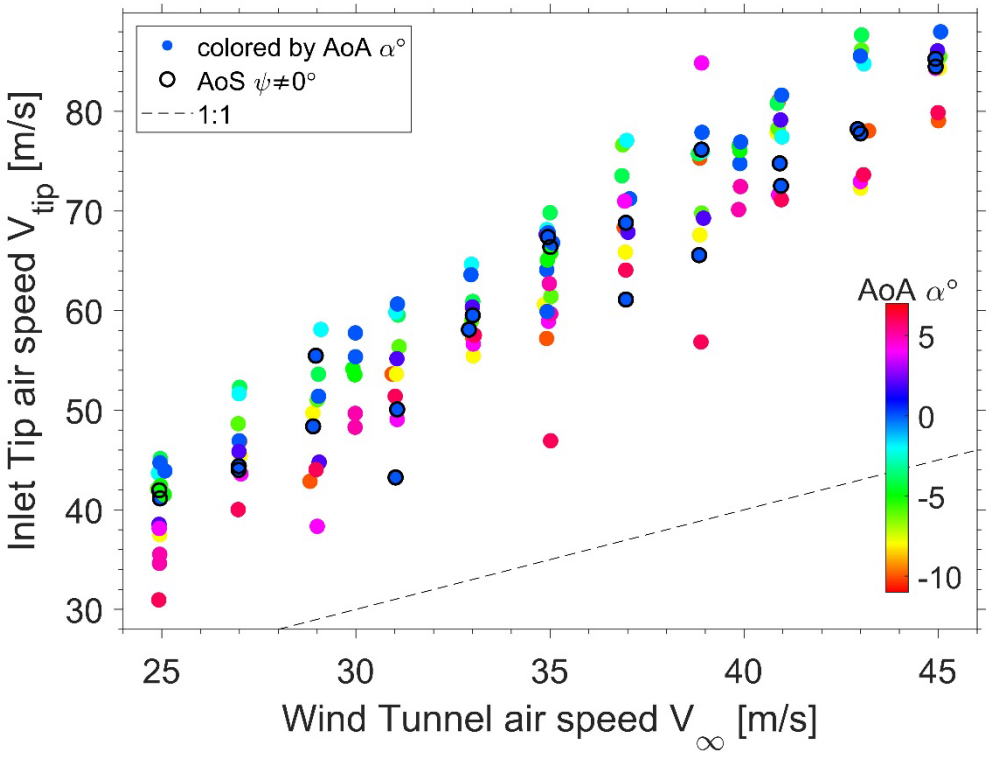

Figure 11. Estimated inlet tip air speed versus wind tunnel air speed. The dots are color coded with angle of attack; black edging marks non-zero angle of sideslip.

The inlet tip air speed slightly depends on angle of attack within a covered range from -10° to +6° (see Figure 12). It stays approximately the same or slightly increases (for lower incoming air speeds) in the range from -6° to 0° and decreases by about 10% at the extremes (-10° and +6°). This dependence may be attributed to changes in scarf efficiency due to different patterns of the boundary layer along the pylon's bottom side. We should remember that the pylon was mounted upside down, so at positive values of angle of attack the front edge of the pylon is higher than the scarf. The air flow following the pylon bottom rotates and becomes "divergent", which slows it down and causes faster boundary-layer growth. Development of flow separation and a recirculation area at the front end of the pylon should be expected at angles of attack above approximately +6°. All of the above makes the scarf less efficient. At negative attack angles similar thing happens at higher absolute values of AoA (about -10°).

Dependence of inlet air speed on angle of sideslip is illustrated by Figure 13. There is almost no change in the inlet tip speed with sideslip angle for lower incoming air speeds (29m/s and below). For higher incoming air speeds, there is no consistency – in some cases the inlet tip speed drops up to 20% when *AoS≠0°* (e. g. V_{air}*=31 m/s*, V_{air}*=41 m/s*); in other cases it stays almost constant (e.g.,V_{air}*=35 m/s*, V_{air}*=45 m/s*).

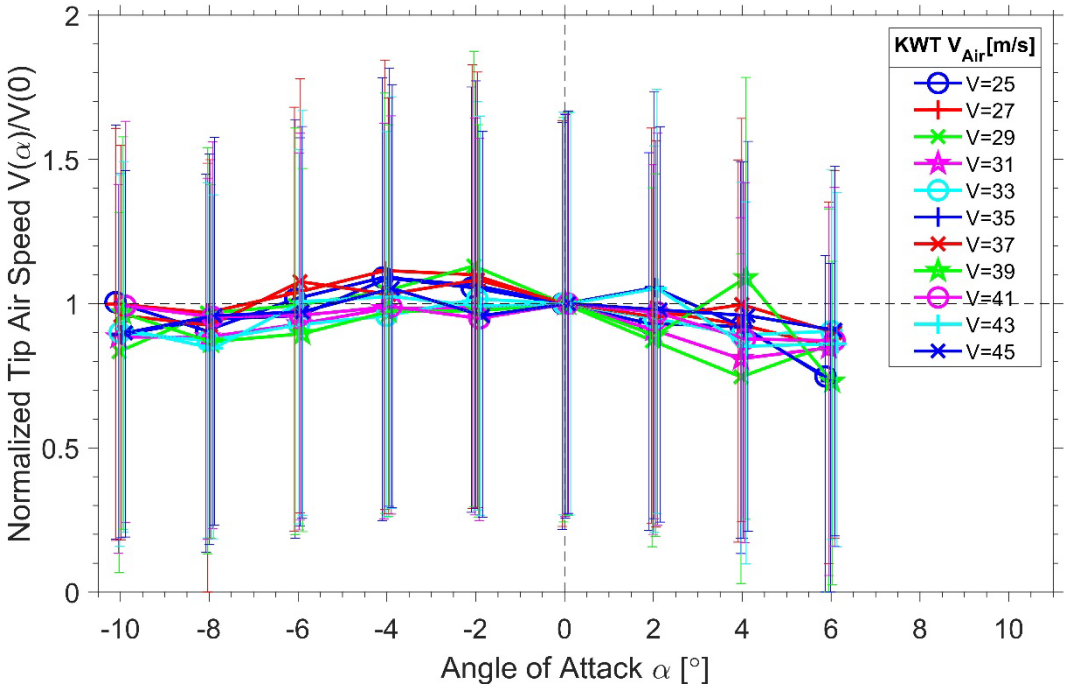

Figure 12. Inlet tip air speed as function of angle of attack. The tip air speed was normalized by speed value at zero angle of attack: V(α)/V(α=0). Nominal incoming air speed is shown in the legend; angle of sideslip was 0 for all plotted data. Vertical bars depict one standard deviation.

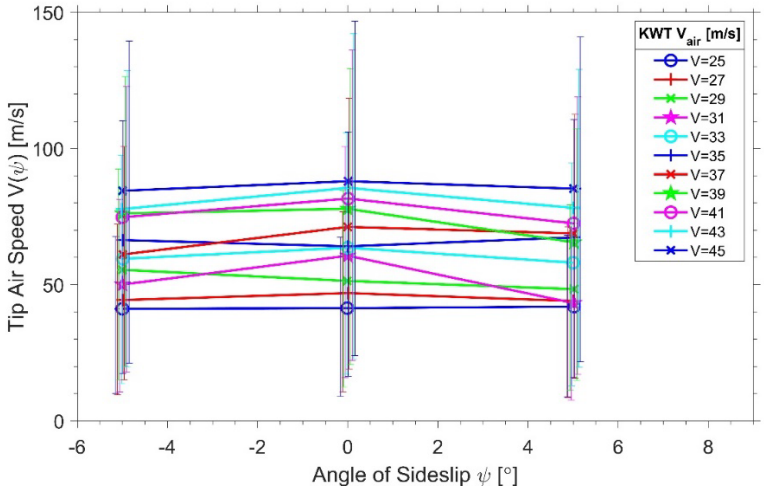

Figure 13. Inlet air speed versus angle of sideslip. Nominal incoming air speed is shown in the legend; angle of attack was 0° for all plotted data. Vertical bars depict one standard deviation.

A scarf performance test was conducted with scarf devices of three sizes (identified as "normal", "smaller", and "smallest") at four air speeds for three angles of attack: 0° and ±5°. All three devices were wedge shaped with 10° angle and rectangular cross-section with rounded corners of the same width, but with different length: 38.1 mm, 25.4 mm, and 12.7 mm, so the back-end cross-sections were 50.8x6.7 mm, 50.8x4.5 mm, and 50.8x2.2 mm correspondingly (see Figure 14).

Figure 14. "Normal" scarf device mounted on the pylon.

The general dependance of the tip air speed on the angle of attack is basically the same as we have seen in specialized tests. There is virtually no dependance of the inlet tip speed on scarf devise size (see Figure 15), which means that even the "smallest" scarf can provide enough vacuum for inlet operation.

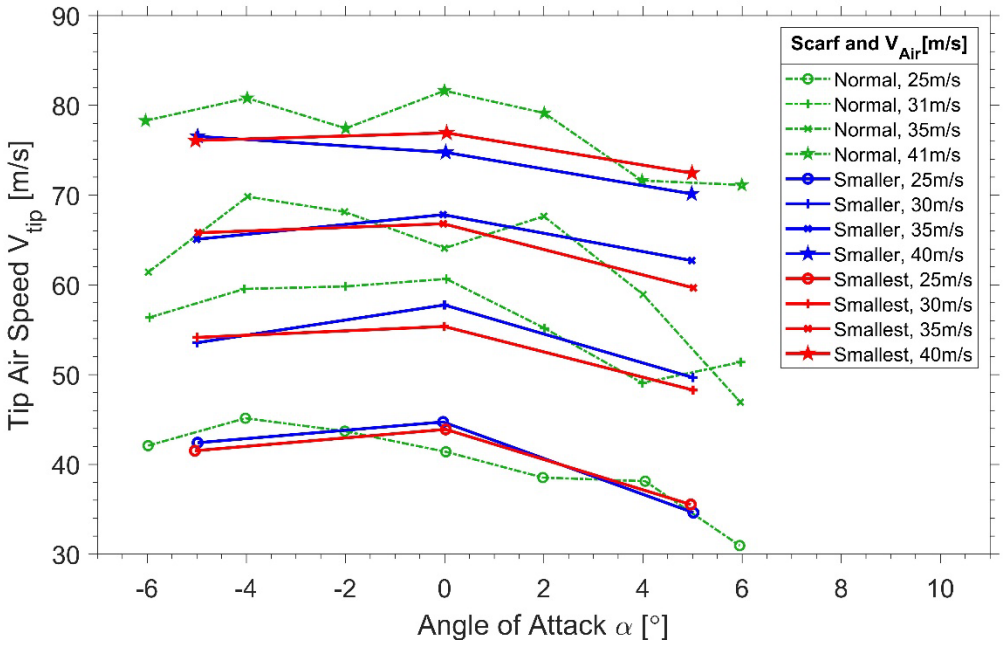

Figure 15. The inlet air speed as a function of angle of attack for three scarf devices.

A smoke test was performed to visually inspect the flow structure around the pylon at a range of angles of attack (-10° to +6°) and sideslip (±5°), and three air speeds (25, 35, and 45 m/s). The pylon's profile (NACA0024) allowed smooth flow along the sides of the pylon at all tested angles of attack and sideslip, and at all tested air speeds; turbulent zone development was detected on the "bottom" side of the pylon at the angles of attack above +4°. We verified that the inlet tip was long enough to sample from the undisturbed air at all tested pylon orientations (see example in Figure 16).

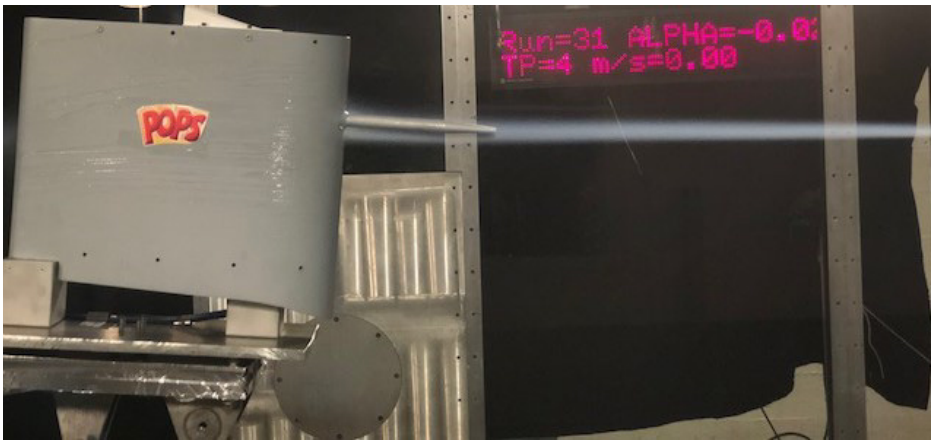

Figure 16. Example of smoke test (AoA=-5°, AoS=0°, V_{air}=40 m/s) − note the inlet tip in the "straight and horizontal" part of the smoke line.

The POPS instrument was running throughout the experiment except for the smoke test. We did not notice any problems with POPS operation except for the well-known problem of very noisy sample flow rate data. We used either smoothed or nominal sample flow value in POPS data processing.

A time series of total aerosol number concentration (Figure 17) shows that the counts dropped over time, which should be accounted for in further analysis to avoid false correlations. Averaged size distributions measured at different AoAs and AoSs show no distortion to the aerosol distribution shape due to inlet misalignment with incoming flow (Figure 18 and Figure 19) or at different incoming air speeds (Figure 20). All three figures contain two panels – the upper one shows POPS data colored by the corresponding variable value (AoA, AoS, or V_{air}) and PCASP data in grey (shown for reference); the lower panel shows PCASP data colored by the corresponding variable value and POPS data in grey. The PCASP data are used to show stability or variation of the background aerosol, so that the changes in POPS size distributions could be properly explained by variations of aerosol parameters or attributed to effects of misalignment or incoming air speed.

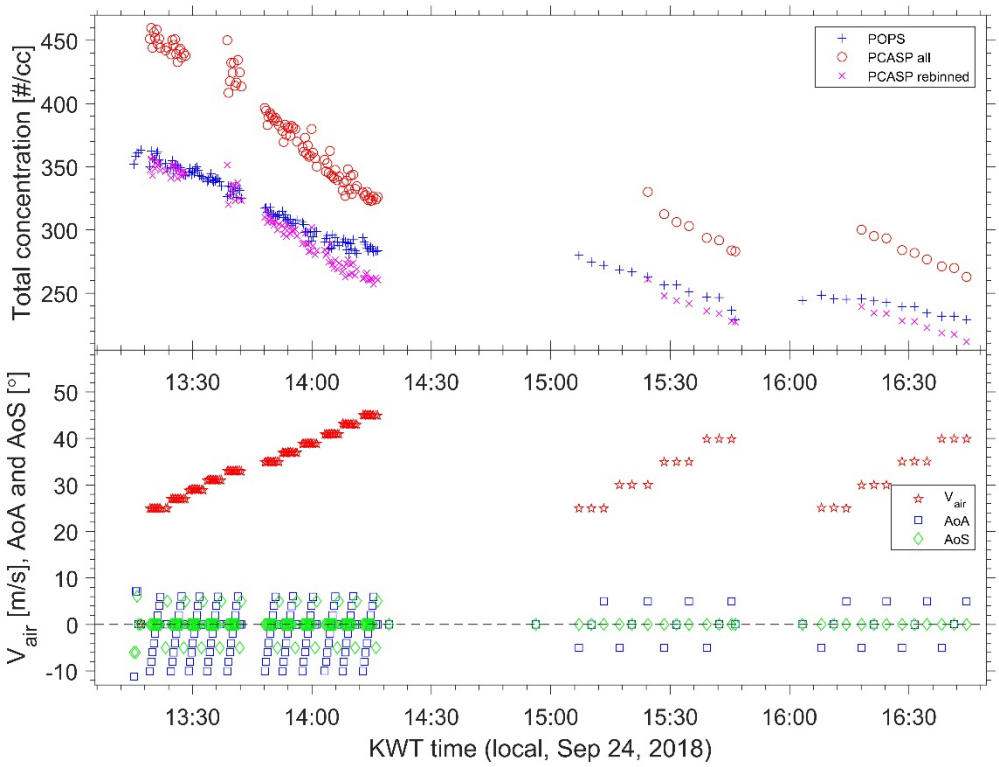

Figure 17. Time series of total aerosol concentration on the upper panel and time series of wind tunnel air speed V_{air}, angle of attack AoA, and angle of sideslip AoS on the lower panel. Magenta 'x' on the upper plot with legend entry "PCASP_rebinned" shows part of PCASP total concentration recalculated over the POPS size range.

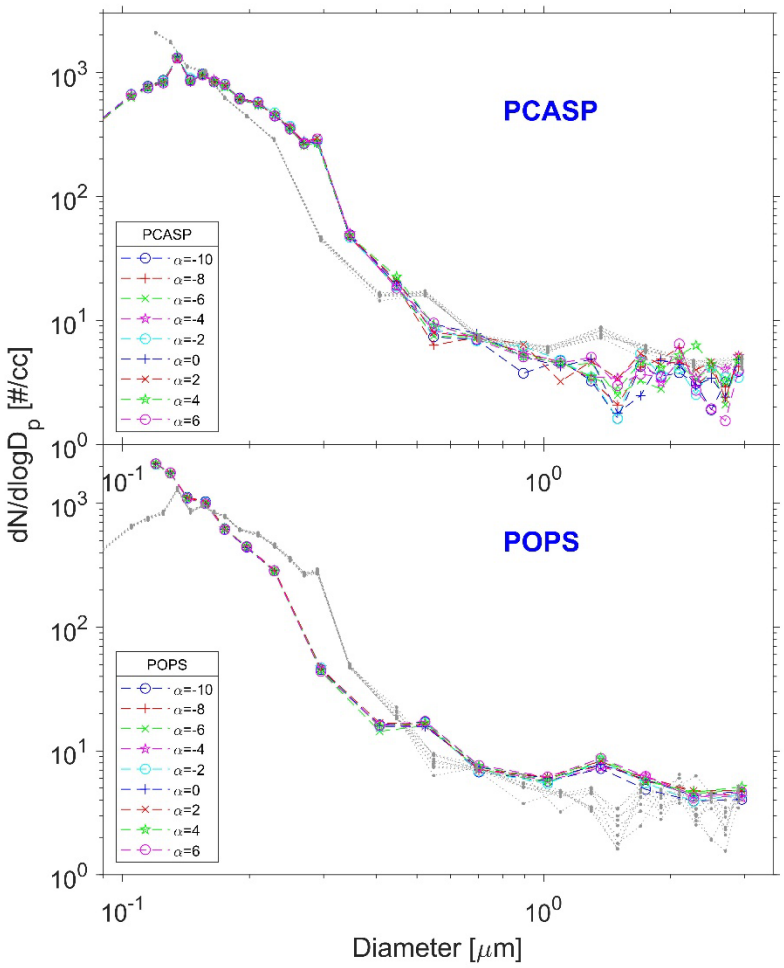

Figure 18. Averaged aerosol size distributions measured at different angles of attack. The upper panel shows colored PCASP averaged size distributions; corresponding POPS data are shown in grey for reference. The lower panel shows colored POPS averaged size distributions; corresponding PCASP data are shown in grey for reference.

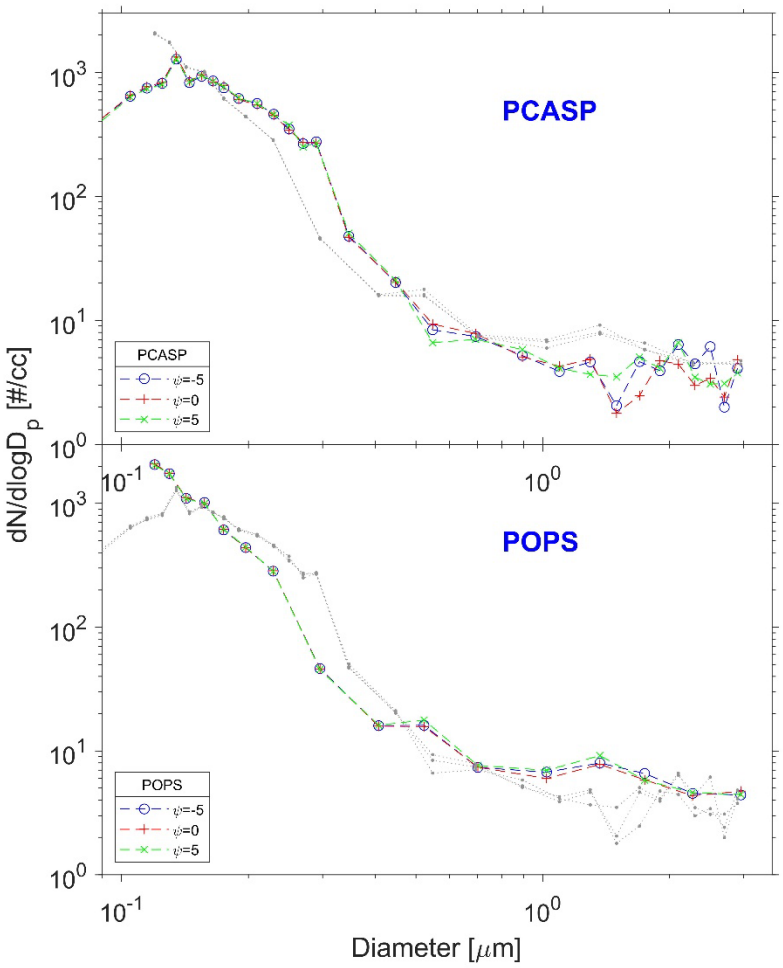

Figure 19. Averaged aerosol size distributions measured at different angles of sideslip. The upper panel shows colored PCASP averaged size distributions; corresponding POPS data are shown in grey for reference. The lower panel shows colored POPS averaged size distributions; corresponding PCASP data are shown in grey for reference.

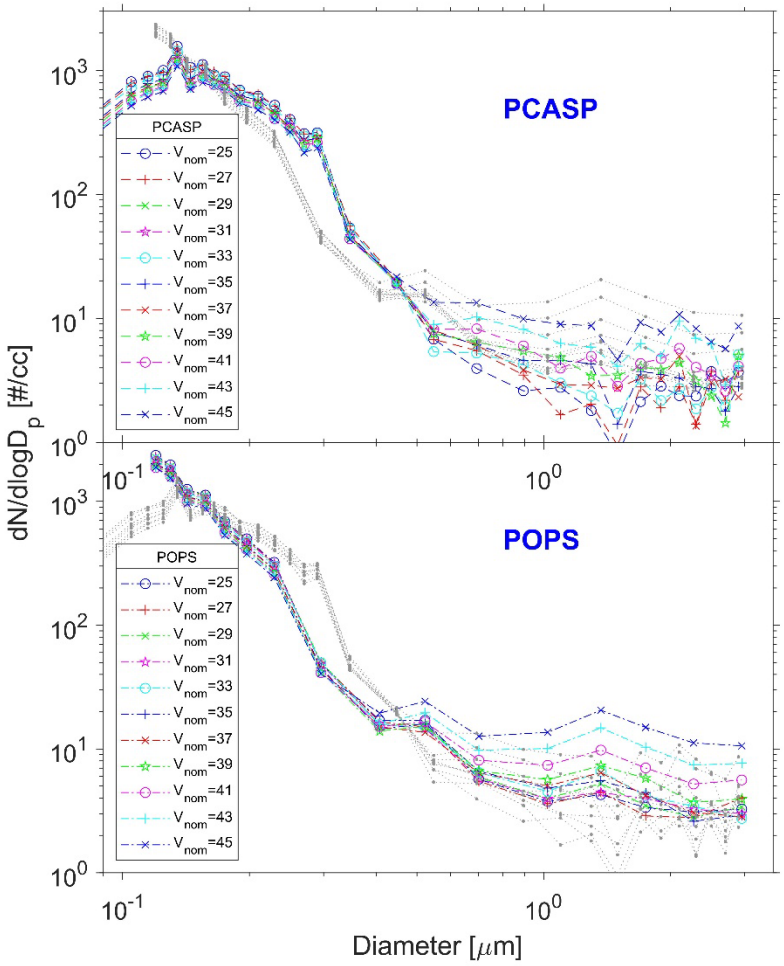

Figure 20. Averaged aerosol size distributions measured at different incoming air speeds. The upper panel shows colored PCASP averaged size distributions; corresponding POPS data are shown in grey for reference. The lower panel shows colored POPS averaged size distributions; corresponding PCASP data are shown in grey for reference.

2.5.3 Flight Test

We performed two flight tests on the ArcticShark in April 2019. The ArcticShark was based in Eastern Oregon Regional Airport (PDT, Pendleton, Oregon) to fly in the Pendleton UAS Test Range airspace (https://pendletonuasrange.com/).

The pylon was mounted under the right wing of the ArcticShark (inner hard point) with inlet and POPS installed inside the pylon. The inlet tip was aligned with the aircraft body horizontal axis, so on the ground it was tilted approximately 3° down, while in flight about 4° up. No flow restriction was used, so the inlet was operated with maximum flow rather than in isokinetic mode (similar to how it was run in the KWT tests).

The AIMMS-30 was mounted under the left wing (outer hard point) parallel to the aircraft axis. Note that the standard data output of the AIMMS probes does not include explicit value of angle of attack, so we calculated our estimate of AoA from available AIMMS data (angle of sideslip, differential pressures for AoS and AoA channels). Since we do not have exact calibration parameters of the AIMMS-30, our angle of attack estimate might be over- or under- evaluated and/or biased, but the relative relationships should remain valid.

The aircraft flight control system (PICCOLO) measures independently the true air speed with a Pitot-static system; these data were used as a second TAS estimate. The AIMMS-30 has a software interlock that blocks output of the air speed and wind data until the TAS exceeds a certain threshold; for cases where we are interested in wider TAS ranges or AIMMS-30 data is not available/valid, we use PICCOLO data.

The ArcticShark payload included a cloud droplet probe (CDP) mounted under the left wing (inner hard point) that can be used to measure coarse-mode aerosols.

Overall, the inlet performed as expected. The flight test results are quite similar to the wind tunnel test results (Figure 21). A major impact on inlet tip air speed was from angle of attack – a substantial drop in inlet air speed is seen on ascent (aircraft angle of attack about +5°, blue markers in Figure 21). The ArcticShark auto pilot controls altitude and speed within certain "corridors" around nominal values, while actual altitude and speed oscillate within these limits (e.g., see Figure 22 for example of TAS distribution). This undulating flight pattern results in substantial changes of the AoA (see Figure 23) and, as a consequence, corresponding change in the tip air flow. On ascent, the AoA is +5.1±1.2° in the range where scarf efficiency drops down (see Figures 12 and 15). Proper orientation of the inlet – according to "nominal" straight-and-level flying AoA (or pitch angle) of the ArcticShark of 4° − should make inlet operation more stable and decrease deviation of the inlet tip air speed from the target value.

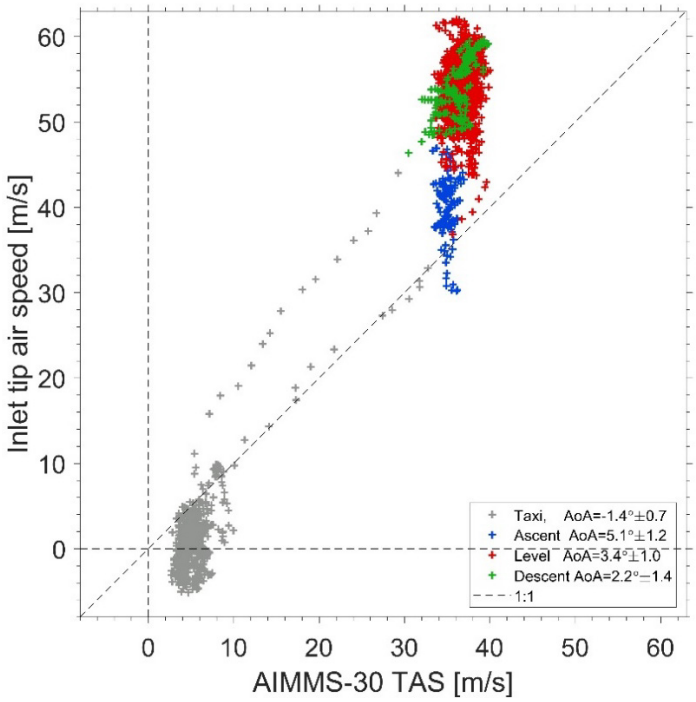

Figure 21. Estimated inlet tip air speed versus TAS (measured by AIMMS-30) for test flight in Pendleton on April 24, 2019. The legend shows average and standard deviation values of aircraft angle of attack (by AIMMS-30).

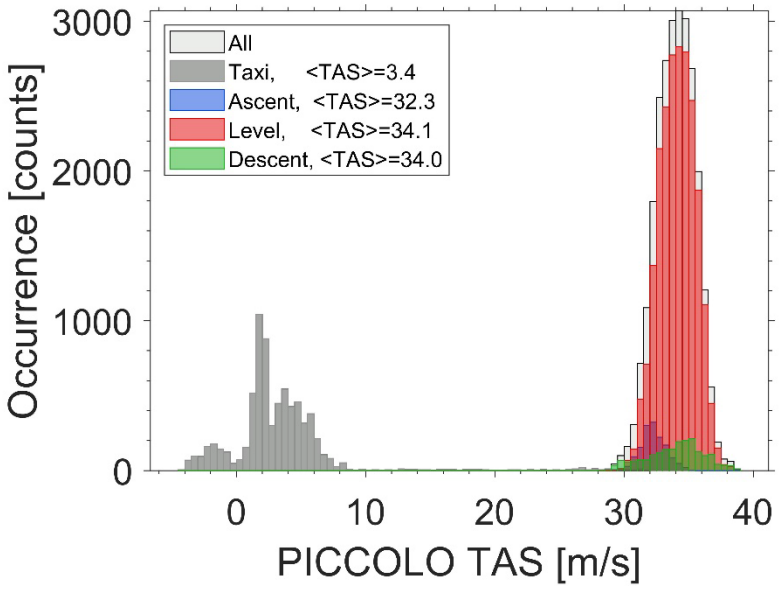

Figure 22. Histograms of the TAS (by PICCOLO) for various parts of the ArcticShark flight on April 24, 2019. Numbers in the legend show mean values of TAS [m/s] for specific parts of flight.

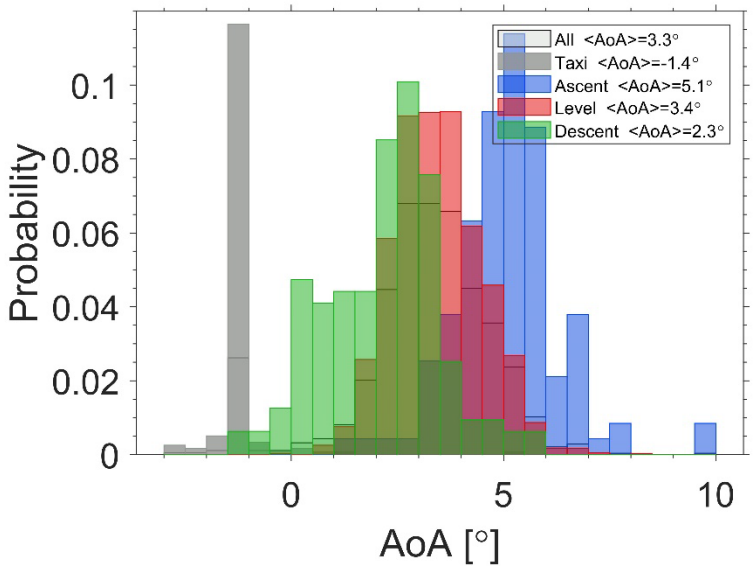

Figure 23. Histograms of the angle of attack for various parts of the ArcticShark flight on April 24, 2019. Numbers in the legend show mean values of AoA for specific parts flight.

An example of POPS-measured aerosol size distribution is shown in Figures 24 and 25. Coarse-mode aerosol size distribution measured by the CDP is plotted in the upper panel of the Figure 24 in "normalized" form (in $dN/dlogD_p$) but in arbitrary concentration units (raw counts) not converted to one of the conventional forms (e.g., #/cc).

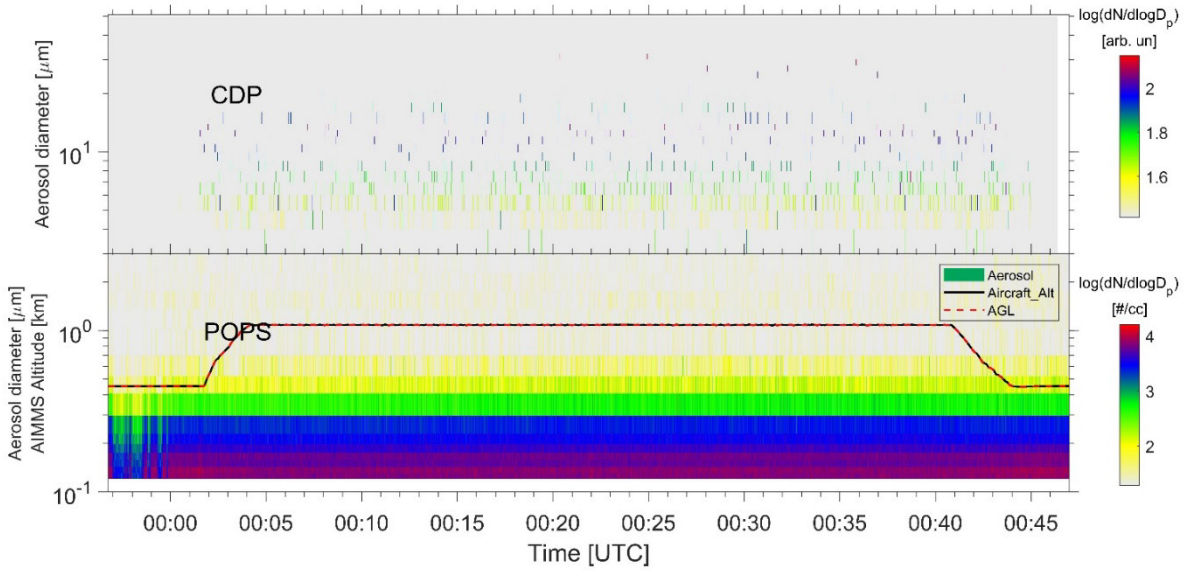

Figure 24. Example of aerosol size distribution measured by POPS and CDP on April 24, 2019. The CDP concentrations are presented in "arbitrary units" since the reported data were "normalized" ($dN/dlogD_p$) but not converted from "raw counts" into customary units (e.g., #/cc). The aircraft altitude is plotted in two versions: the solid black line is based on AIMMS-30 data; the red dashed line shows the autopilot data.

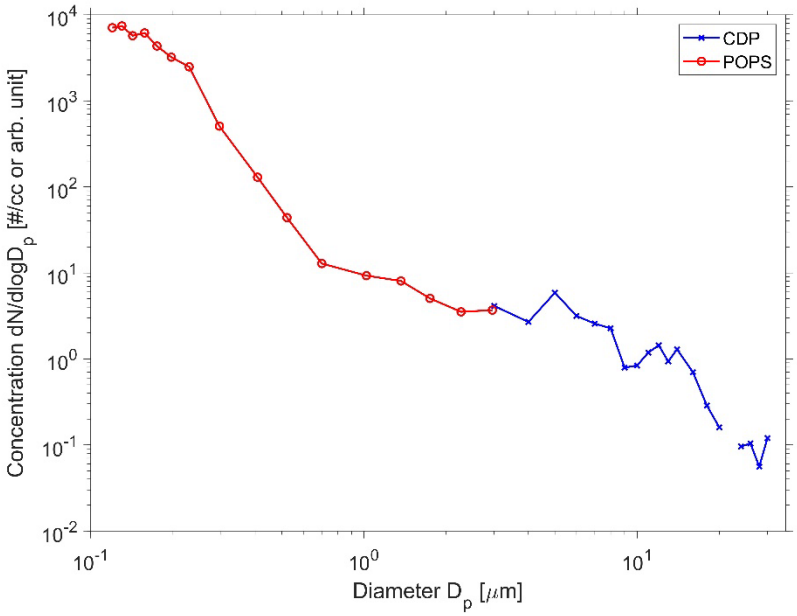

Figure 25. Example for aerosol size distribution measured by POPS and CDP on April 24, 2019. The distributions were averaged for the section of the flight at one elevation. The CDP concentrations are presented in "arbitrary units" since the reported data were "normalized" (dN/dlogD$_p$) but not converted from "raw counts" into customary units (e.g., #/cc).

2.6 Concluding Remarks and Recommendations

The designed POPS pylon inlet has met or exceeded the required parameters. Our simple “flow resistance” analysis of the inlet showed the main feature of the inlet: self-regulating over a wide range of platform speeds. Experimental tests confirmed analysis conclusions and provided necessary “real-world” information for fine tuning of the inlet.

For real deployment, the inlet flow rate should be restricted with an orifice near or incorporated into a scarf device. Orifice diameter should be adjusted in a “try and see” approach over several test flights.

The other option of inlet flow control – varying the size of the scarf device – seems to be less practical because (a) efficiency of the scarf strongly depends on misalignment of incoming flow (combination of angle of sideslip and angle of attack); (b) manufacture of scarf devices of several sizes for fine tuning in a “try and see” manner might be not practical.

We advise selecting an inlet flow rate to have near-isokinetic sampling conditions – flow decrease at extreme angles of attack should cause slight under-kinetic sampling that should not noticeably affect inlet collection efficiency. The inlet tip should be tilted down by an angle equal to the angle of attack most common for straight-and-level flight.

The approach taken for the current inlet – passive inlet with scarf device and flow rate far exceeding flow rate of the sampling instrumentation – could be used in design of inlets for other small UASs or for sensors with special sampling requirements (e.g., chemically inert inlet material). The current design

allows for distributed arrangement; for example, some parts of the inlet (e.g., flow meter or scarf device) might be placed far away from other parts and connected with a long, not necessarily straight, line.

The scarf devices are capable of much higher vacuum suction than required for the current inlet implementation, which eases one requirement on the flow meter – minimum pressure drop. The Venturi flow meter might be replaced with another standard or off-the-shelf meter − like a laminar flow element (LFE) or even an inline meter like the TSI 4200 series.

To repeat, very concisely, the logical chain of calculations for the key diameters of the inlet:

- Initial parameters ("given" or commonsense values): platform speed V_∞, aerosol sensor sample flow Q_s and inlet line ID D_s, critical Reynolds number Re_{cr}, Venturi contraction coefficient c_r, if Venturi flow meter is planned.
- The air speed in the main inlet tube V_m should be the same as the air speed in the sensor sample line V_s (isokinetic sampling), which is calculated from the sensor flow and line diameter: $V_m = V_s = 4Q_s/\pi D_s^2$.
- Main tube diameter D_m is calculated based on the requirement of laminar flow in the Venturi contraction, i.e., local $Re \leq Re_{cr}$: $D_m \leq Re_{cr}\nu/V_m c_r$. If a flow meter of different type is planned, then the requirement on main tube diameter may be relaxed to $D_m \leq Re_{cr}\nu/V_m$ (laminar flow in the main tube).
- Total inlet flow is calculated from the main inlet tube air speed and diameter: $Q_m = V_m \pi D_m^2/4$.
- Inlet tip orifice diameter is calculated from the inlet flow using isokinetic condition at the tip ($V_{tip}=V_\infty$): $D_t = \sqrt{4Q_m/\pi V_\infty}$.

After the base diameters D_m, D_t, and D_c were calculated, one diameter might be adjusted for some other reasons (e.g., ease of manufacturing, "standard fraction" value in imperial units, standard tube size, etc.); if so, then all other parameters have to be reassessed. Linear dimensions of the inlet parts could be established using base diameters and commonsense considerations to keep the flow in laminar state and place the inlet tip in the undisturbed air upstream of the platform.

At the time of writing, the POPS pylon inlet design has been placed on hold since the POPS sensor is currently mounted in the aircraft instrumentation bay as a part of PNNL standard aerosol payload and there are no plans for deploying the POPS in the pylon.

3.0 Community Aerosol Inlet for a Suite of Diverse Instruments

3.1 Requirements

The current ARM Aerial Facility (AAF)/PNNL payload for a UAS is a collection of diverse instruments including remote-sensing optical instruments (e.g., multi-wavelength camera), a suite of aerosol instrumentation (condensation particle counter, optical aerosol spectrometer, aerosol absorption photometer, sample filter collector), a trace gas sensor (CO_2/H_2O infrared gas analyzer, IRGA), and a meteorological package (AIMMS-30). Aerosol and trace gas instrumentation needs an inlet system to

draw the air sample and transport it to the sensors. However, requirements to the sampling conditions vary: while IRGA needs filtered air at a specific flow rate, the aerosol instrumentation requires isokinetic sampling to avoid distortions to the aerosol size distribution and concentration. Most aerosol instrumentation requires humidity control (drying) of the sample flow, except the aerosol filter sampler that works with unconditioned air. While most instruments are equipped with internal pumps, they still may require special plumbing arrangements to minimize the pressure difference between the inlet and exhaust lines; few instruments are pumpless and rely on an external vacuum source.

As a starting point for inlet development, we compiled the following list of requirements (capabilities and features) for the designed inlet:

- Near-isokinetic sampling at cruise speeds of the TigerShark UAS family (including ArcticShark). NOTE: the aircraft is controlled in terms of indicated air speed, while the inlet has to deal with true air speed; the relation between these two speeds depends on altitude, e.g., at sea level they coincide, while at 5500 mMSL (nominal ceiling for the ArcticShark) ArcticShark loiter IAS of 68kt (35 m/s) corresponds to TAS of 90 kt (46 m/s).
- Minimal distortion to the size distribution and total concentration, as well as minimal particle losses for aerosols with sizes 0.05 through 2 μm.
- Provide about 7 SLPM sample flow for a heterogeneous set of sensors.
- Efficient humidity conditioning (drying) for aerosol counting, sizing, and optical properties instruments.
- Direct measurement of the total inlet flow by non-disturbing meter (e.g., based on Venturi tube).
- Active flow control either in automated or manual mode.
- Laminar flow in most parts of the inlet.
- Inlet tip long enough to sample in the undisturbed air upstream of the aircraft body (about 2x body width).
- Minimal weight.
- Adaptable enough to fit confined space or allow distributed arrangement of the parts.
- Simple and cost effective for manufacture, duplication, and adjustment.

3.2 Design Inputs, Assumptions, and Considerations for Determining Operational Parameters and Physical Dimensions

We used the same approach for the design of this community inlet as for the POPS pylon inlet: an iterative process, starting from a list of requirements and certain commonsense assumptions, then calculation of specific dimensions and values using parameters and constraints from the list of requirements. If the result does not answer all requirements, we adjust the initial parameters and repeat the process. As we gain experience with the inlets and real-world data, we use it to augment or replace commonsense assumptions in the design.

The general layout of the inlet was chosen as follows:

- Inlet tube with front cone at the tip; the cone expansion angle small enough to avoid flow separation from the walls (below 11°, no turbulent and/or recirculation zones)
- Main inlet tube long enough for the laminar flow to form/develop in the tube and to place the inlet tip far enough off the aircraft body in undisturbed air flow
- Flow meter optimized for minimal flow disturbance and aerosol losses
- Two-way flow splitter to separate a portion of the sample flow that requires humidity conditioning (drying) from unconditioned part
- Nafion dryer installed in vacuum reflux split flow configuration (so called “poor man’s configuration” when part of the dried flow is used as a purge flow, no special source of dry purge gas)
- Network of conductive lines, flow splitters, and pickoffs to provide all instruments with the necessary air (sample, sheath, and dilution flows) and convenient exhaust, if necessary
- Mass flow controller for controlling a bypass flow to balance total flow either at fixed (nominal) value appropriate for the current altitude or dynamically, according to actual true air speed
- Vacuum pump capable of handling the expected inlet flow range and maintain a pressure drop large enough to sustain choked flow in the critical orifices
- The main parts of the inlet upstream of any aerosol sensor are supposed to be connected with either metal or black silicon conductive tubing of appropriate size to minimize particle loss via electrostatic deposition.

3.2.1 Main Inlet Tube

The choice of the size for main inlet tube is governed by several contradictory requirements: the smaller diameter, the shorter the residence time (and the smaller gravitational deposition of the aerosols), but diameter should be large enough for maintaining laminar flow and having enough structural strength with reasonable weight for a rather long inlet tube necessary to sample in the undisturbed air upstream of the aircraft body. Standard aluminum thick-wall pipe with OD=0.695” (15.88 mm) and ID=0.495” (12.57 mm) seems to be a reasonable trade-off for these requirements. In a tube of this size the air flows below 17LPM should be stable laminar (Re<2000) and transition from turbulent to laminar regime (e.g., in the cone at the tip) should happen very fast.

Inlet tip main tube length is defined by requirements to sample in the undisturbed air (the longer the better), development of laminar flow (the longer the better), structural strength (the shorter the better), sample residence time (the shorter the better), and practical use (too long a tip is difficult to work with or around). The tube length was chosen to be about 25 cm for the TigerShark and about 45cm for the ArcticShark.

3.2.2 Flow Meter (Venturi Tube)

A flow meter based on a Venturi tube seems to be the best choice to measure total flow in an aerosol inlet upstream of the instruments. Among all pressure differential flow meters, it causes minimal disturbance to the flow and aerosol population, and has good sensitivity within a decent dynamic range. A major

drawback of a Venturi tube is that it is not universal: its dimensions should match the main line diameter; hence, it should be manufactured for a specific tube size. International Standard ISO-5167-4 recommends that the ratio of the main line diameter to the throat diameter be within 2 and 4. This is a tradeoff between disturbance to the flow (the lower the better) and sensitivity (the higher the better). We used a value of 2 to minimize distortions while maintaining decent sensitivity.

Another consideration is to have the Venturi throat as large as possible to avoid development of a local turbulent zone. Transition to turbulence in tube flows happens for Reynolds numbers between 2300 and 4000, depending on wall roughness and flow prehistory (turns, channel shape/cross-section change, etc.). For our choice of the main tube (ID=12.57 mm) and contraction ratio of 2, the throat flow remains laminar up to about 10 LPM (Re<2300), and probably well beyond since the inlet walls are very smooth, the throat is very short, and the flow upstream of the Venturi tube is straight and stable long enough to become fully developed laminar flow.

3.2.3 Inlet Tip (Front) Cone

The inlet tip (front) cone expansion angle was chosen to be 10°, the same as for the POPS pylon inlet. Inlet tip orifice diameter can be estimated from nominal platform speed (35 m/s for ArcticShark) and maximum allowed Reynolds number ($Re_{max}=2300$) in the Venturi throat ($ID=6.29\ mm$) as $D_{tip}=2.49$ mm. We chose an inlet tip orifice diameter $D_{tip}=2.54$ mm (0.1") to simplify inlet cone manufacture and some ballpark estimates (the front cone expansion ratio becomes simple 5, etc.).

Nominal inlet flow rates for the chosen inlet tip orifice D_{tip} at nominal cruise speeds of ArcticShark (35 m/s IAS) and TigerShark (30 m/s IAS) are 10.6 LPM and 9.1 LPM correspondingly at sea level. For an operational ceiling of 5500 mMSL the TASs are 46 m/s and 38 m/s with corresponding flows of 14 LPM and 11.7 LPM.

3.2.4 Nafion Dryer

The current PNNL payload for a UAS consists of remote-sensing optical instruments (e.g., multi-wavelength camera), a suite of aerosol instrumentation (condensation particle counter, optical aerosol spectrometer, aerosol absorption photometer, filter sampler), and a trace gas sensor (CO_2/H_2O infrared gas analyzer). Aerosol and trace gas instrumentation sample from the inlet; however, only a subset of the instruments require humidity control (drying) of the sample flow − the IRGA, aerosol filter sampler, and bypass MFC work with an unconditioned air sample. Nominal net flow to be dried is expected to be 2.52 LPM, while total flow required by the instruments (including drier purge flow) is 6.02 LPM.

From our experience with Nafion driers on DOE's Gulfstream-1 aircraft, a 12-inch-long monotube drier model MD-700 (by PermaPure) should be adequate for the anticipated flows to lower relative humidity below 40% in most cases. The drier has to be installed in vacuum reflux purge flow configuration with purge flow controlled by a critical orifice in the upstream port. Placing the control element (critical orifice) at the entrance of the purge flow path puts the purge flow at very low pressure (almost down to vacuum pump inlet pressure), which further lowers humidity of the purge air, improving performance of the drier.

The MD-700 was specifically designed for aerosol applications to minimize losses of aerosols and/or volatile particulate components: single 17mm-diameter Nafion tubing, stainless-steel tube and shell construction, etc. (details are available on the manufacture's web site http://www.permapure.com/products/gas-sample-dryers/md-700-series-dryer-for-aerosol-analysis/). Purge flow limited by 1LPM critical orifice should be sufficient for our application. For example, if we assume vacuum pump pressure to be about 1/5 of ambient, then the volumetric sheath flow is about 5 LPM, twice as large as the anticipated sample flow, which makes sub-second residence time for purge air in a 12-inch unit.

3.2.5 Bypass Flow

The total flow through the inlet Q_{inl} is determined by the TAS (if isokinetic condition is maintained). Part of the flow is drawn by instruments and the drier; however, the total should be balanced by bypass flow $Q_b=Q_{inl}-(Q_h+Q_n+Q_d)$ where $Q_h=2.52$ LPM is the net flow for the instruments with humidity control, $Q_n=3.5$ LPM is net flow for the instruments without humidity control, and $Q_d=1$LPM is drier sheath flow. For nominal speeds and assumed inlet geometry Q_{inl}, values are 10.64 LPM for ArcticShark (35 m/s) and 9.12 LPM for TigerShark (30 m/s); corresponding bypass flows are 3.62 LPM and 2.10 LPM.

We chose an Alicat mass flow controller (MC series, 10LPM range) with a control valve downstream of the internal sensors. This control valve location allows the MFC to be used in volumetric flow control mode with reference to upstream pressure and temperature. Alicat MFCs are fast and precise controllers. Inherently, they work in volumetric flow mode; mass flow mode is implemented via corrections in the firmware. The flow range has been chosen to be large enough so that the MFC could keep the inlet in an isokinetic state for most altitudes even if all instruments are not operational (not drawing any flow). On the other hand, the range is not so large that the MFC loses decent precision and resolution. The chosen range also gives good margin in case we need increase total inlet and/or net instrument flows.

3.2.6 Operational Modes

Two operational modes are possible for the Community Aerosol Inlet: constant flow and TAS tracing modes. In TAS tracing operational mode, the bypass flow is adjusted in real time to match the total inlet flow with a value calculated from the current TAS. The flow adjustments could be done in two styles: (1) "nominal" style – new bypass flow is calculated from nominal flows of all instruments and TAS; (2) "real" style – change to the current bypass flow value is calculated as the difference between total flow value calculated from the current TAS and current total flow value measured by the Venturi meter. For both styles, the inlet control program needs real-time true air speed, which could be obtained from another datastream (e.g., AIMMS-30) or measured with a designated sensor. There is another condition for "real"-style flow adjustment – Venturi measurement of the total inlet flow must be fully corrected for local conditions (temperature and pressure) – that requires accurate measurement of absolute pressure and temperature of the air in the inlet.

In constant flow operational mode, the bypass flow is manually adjusted to match current or nominal TAS once or a few times per flight − e.g., after substantial altitude changes. As noted above, the aircraft control is based on indicated air speed rather than on true air speed. For our range of speeds and altitudes, they can be related via air density as $TAS = IAS\sqrt{\rho_0/\rho}$ where subscript zero denotes air density at sea level in the International Standard Atmosphere (15°C and 1013.25 hPa, corresponding to a density of

1.225 kg/m^3). The "cruise" TAS increases with altitude: for example, TigerShark "nominal" *IAS=30* m/s translates into *TAS=33* m/s at 2000 mMSL and into *TAS=37* m/s at 4000 mMSL.

The question of which operational mode is better for our application still remains open: constant flow mode is simple and stable, deviation from isokinetic state is within reasonable limits, and it basically does not require the data acquisition computer (DAQ) for operation (just for recording), while TAS tracing mode is much more complex to operate, requires careful programming, real-time data exchange among several devices/programs, could be prone to natural oscillations (as any automated system with feedback), and still cannot guarantee 100% isokinetic sampling due to the inherent response time of the sensors and delays in data exchange.

3.2.7 Software, Prototyping of a Controller

As of the time of writing, the Community Aerosol Inlet development is still work in progress and the inlet is not finalized. The next modification to the inlet will be based on our experience and collected data.

Currently, the inlet is implemented as a collection of autonomous parts that work independently, rather than as an integrated device with unified control. The main payload DAQ runs several independent programs that record/plot the data from Venturi pressure and several T/RH sensors, capture the AIMMS-30 datastream, and record/plot/control the MFC. However, there is no interaction or data exchange among these programs, which is necessary to operate in TAS tracing mode.

There are two main options to unify the inlet control: (1) make a single program on a DAQ computer to read the sensors' data (either from sensors directly or from the datastreams), calculate response, and control the bypass flow (operate the MFC), or (2) delegate this functionality to a dedicated controller or single-board computer and leave only data record and plotting for the DAQ or for the operator's computer in the mobile operation center (MOC). Both options require TAS values to be supplied to the program/controller in real time if the inlet is to be operated in TAS trace mode. The TAS could be measured by a dedicated sensor integrated into the inlet system (new part, needs design and integration), or retrieved from the AIMMS-30 real-time datastream (needs modification to the AIMMS-30 real-time data-capturing program on the DAQ computer). It should be noted that the IAS is measured by the Pitot-static system (part of the aircraft control) and used by the autopilot to fly the aircraft. However, the real-time data from the autopilot system is not available with the current avionics/software.

We tested a prototype controller system based on an Arduino Mega board in several test flights. The Arduino Mega is designed around a 16-MHz 8-bit microprocessor with about 256 KB memory for code; it directly supports SPI and I2C interfaces and has four onboard UARTs for serial communications.

We programmed the board to read the data from three pressure sensors (two differential and one altimeter) via a I2C interface at 100 Hz and averaged it to 10 Hz. The bypass flow MFC was polled at 10 Hz and averaged to 1 second. A dedicated serial channel was monitored for real time TAS value (to be supplied by an external source). A new bypass flow value was calculated at 1 Hz and, if different from the current one, the MFC was re-programmed. The system used a third serial interface to send out an interlaced datastream: averaged pressure and raw MFC data at 10 Hz and averaged flow, TAS, and MFC data at 1 Hz. The operation time base of 100/10/1 Hz was definitely overkill for an inlet on a slow-moving and rather stable platform; it was chosen to challenge the limits of the microcontroller.

This prototype system worked in parallel with the current inlet hardware/software to mimic real operation using real sensors/data in real flight with all precautions taken to cause no interference to inlet operation. The bypass MFC set point was not changed, but was reprogramed with a nominal value.

The main purpose of this exercise was to check feasibility of a microcontroller-based inlet control system. The system worked as expected: no missed cycles or data drops were noted. Our code was not optimized or "polished" and contained unnecessary diagnostic parts; however, the execution module occupied less than a half of available memory. Unoccupied memory could be used to implement basic network functionality to pass the data via UDP packets (the preferred way in the current DAQ system) and/or add local data storage capability (flash card). This example shows that even a cheap, low-power, dedicated microcontroller could be used to build a fully functional inlet control system.

3.2.8 Aerosol Collection Efficiency of the Inlet

The collection efficiency of the Community Aerosol Inlet was estimated using Particle Loss Calculator for a nominal platform speed (30 m/s for TigerShark) and aerosol density of $\rho_p=1.0\ g/cm^3$ (water/ice) or $\rho_p=1.7\ g/cm^3$ (typical value for ambient, organic-dominated aerosols). Describing aerosol instrumentation, the collection efficiency of which depends on aerodynamics, it is customary to use equivalent aerodynamic size (tied to aerosol density of $\rho_0=1.0\ g/cm^3$). In the calculations, we considered only the front part of the inlet, upstream of the first flow splitter (inlet tip, main tube, and Venturi flow meter); the network of lines to transport the sample to the sensors has to be evaluated separately.

Dependance of the inlet transmission efficiency on true air speed is illustrated by Figure 26 (air flow angle is 0°, inlet flow rate is "nominal" for TigerShark cruise speed); black dots/line depict an isokinetic case. The insert in Figure 26 contains a blown-up part of the main plot to show details in the 95 to 101% efficiency range. For all cases shown, the 50% cut size is above 1 0µm. There is negligible (below 1%) overestimation of aerosols in a size range of approximately 0.6 µm to 3 µm in a super-kinetic regime. The upper cut size value shifts down as TAS drops, but even in the worst case ($TAS\text{-}V_{tip}=-2.5\ m/s$) the collection efficiency is above 95% for particles up to 1.3 µm.

Implications of flow misalignment with inlet tip axis are illustrated by Figure 27. With flow angle increasing, the 50% cut size shifts down, but even for 11° it is still well above 10 µm. Limited flow misalignment (up to about 10°) has a minor effect on collection efficiency of the Community Aerosol Inlet.

Several arbitrarily chosen "worst-case" scenarios are shown in Figure 28. Super-kinetic conditions lead to overestimation of larger aerosols, up to 15% for 5-6 µm particles in case of very low inlet flow rate (56% of nominal) and higher TAS (green dots on the plot). Under-kinetic conditions, especially combined with misalignment, shift down the upper cut size: at a level of 50% it changes from about 18 µm to 6 µm; 95% cut size drops from about 5 µ to 0.7 µm.

The collection efficiency calculated for three aerosol densities of 1.0 g/cm^3(ice/water), 1.7 g/cm^3 (organics-dominated ambient aerosol), and 2.4 g/cm^3 (generic mineral dust) are shown in Figure 29. For the heaviest particles, the 50% cutoff size drops to 7.5 µm.

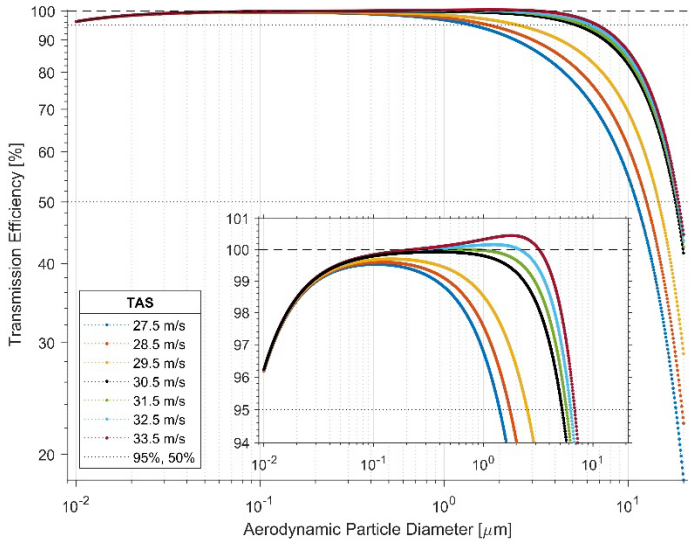

Figure 26. Community Aerosol Inlet collection efficiency estimate with Particle Loss Calculator for aligned flow (air flow angle of 0°) and a range of true air speeds. Black dots/line show isokinetic case.

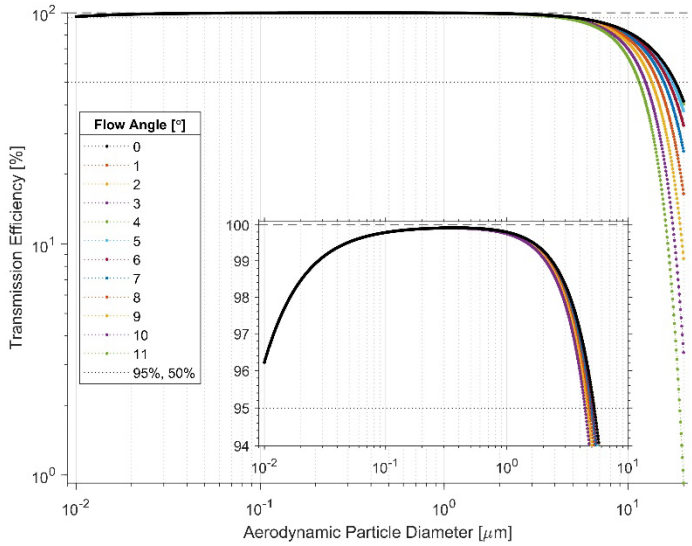

Figure 27. Community Aerosol Inlet collection efficiency estimate with Particle Loss Calculator for misaligned flows for "nominal" TAS and matching inlet flow rate. Black dots show aligned and isokinetic cases.

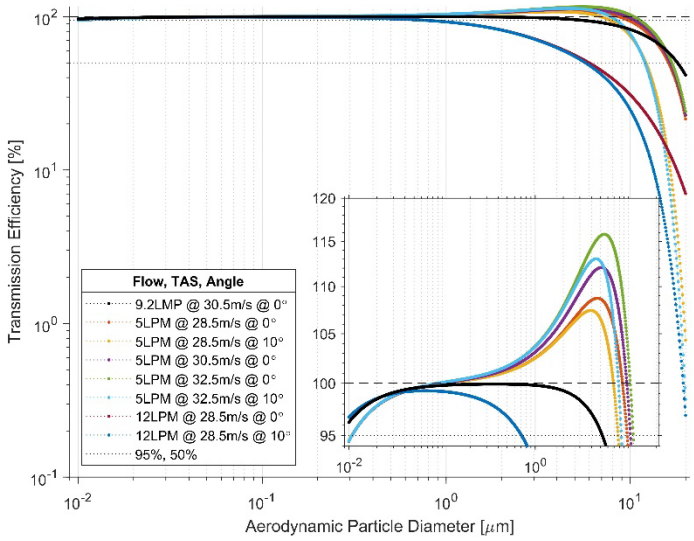

Figure 28. Community Aerosol Inlet collection efficiency estimate with Particle Loss Calculator for several "worst-case" combinations of TAS, inlet flow rate, and misalignment. Black dots show "nominal" case (isokinetic, perfectly aligned).

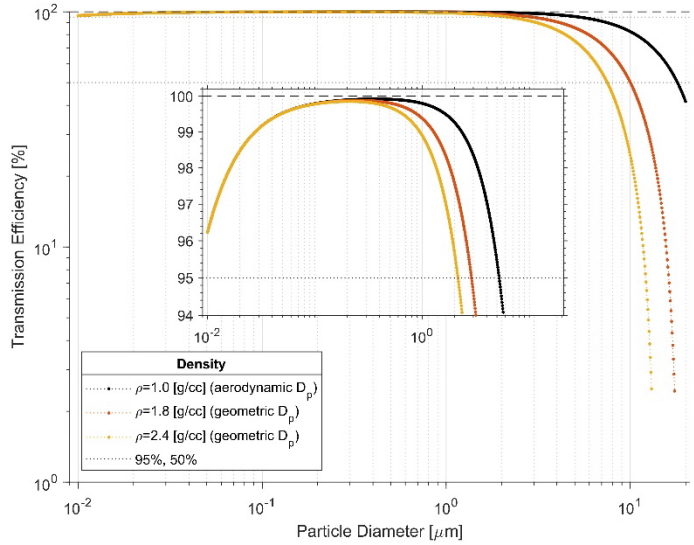

Figure 29. Community Aerosol Inlet collection efficiency estimate Particle Loss Calculator for three aerosol densities.

3.3 Flight Tests

We tested the Community Aerosol Inlet on the University of Mississippi Raspet Flight Research Laboratory TigerShark during three deployments: two in Mississippi (payload integration and initial flight tests in March and June, 2021) and one in Oklahoma (scientific capability showcase in November, 2021).

3.3.1 Inlet Tip Orientation: Tilt Estimate and Adjustment

The inlet main tube was mounted 4° down according to expected nominal pitch angle of the TigerShark at straight-and-level flight. The AIMMS-30 probe was mounted below the right wing, tilted at the same 4° down. Alignment of the inlet main tube with incoming air was checked with the help of a five-port gust probe (3-mm AirData Probe, by Aeroprobe Corporation, Virginia) in a special flight on November 8, 2021, over the ARM Southern Great Plains (SGP) atmospheric observatory. The probe was mounted in place of the inlet main tube so that the tip of the probe was in the position of the tip of the inlet.

This flight was dedicated to (1) calibration of the AIMMS-30 probe and (2) measurement of the angle of attack near the Community Aerosol Inlet tip position. Calibration of the AIMMS-30 involves a set of specific maneuvers and, unlike normal research flight, time spent on "straight-and-level" legs was minimal (see Figure 30), so we based our analysis on statistics for "level" flight only, which includes turns and circulations.

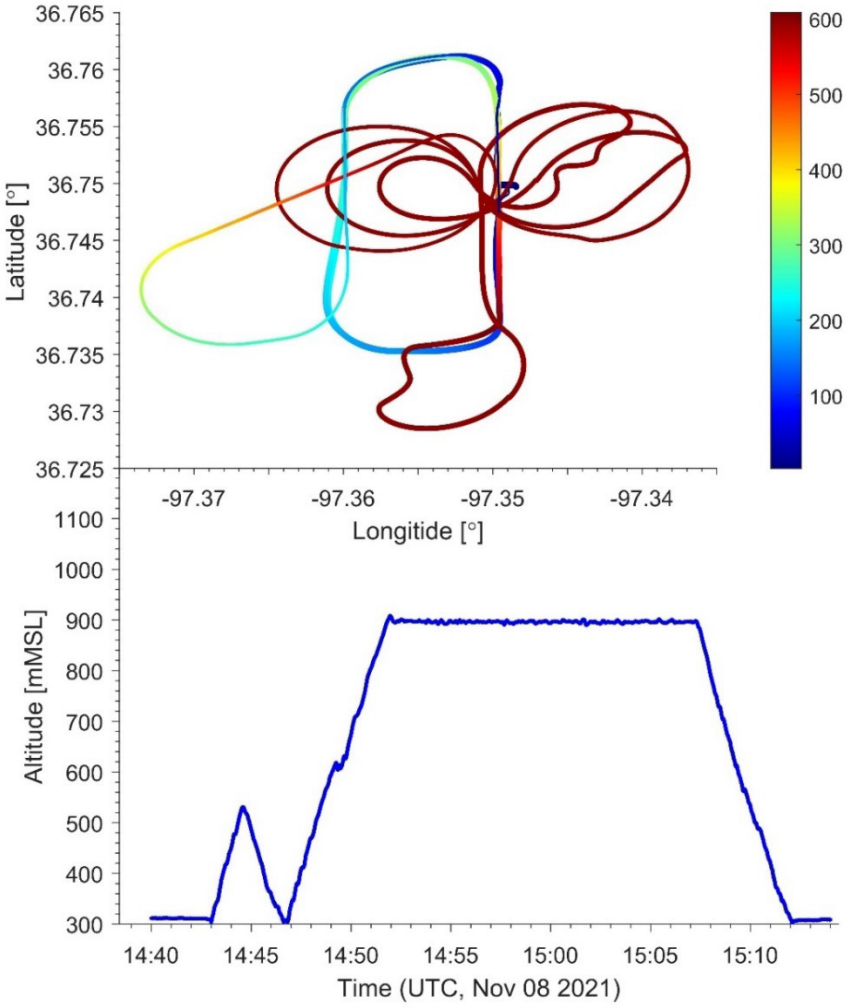

Figure 30. Ground track and elevation profile for the calibration flight of the TigerShark at the SGP on November 8, 2021. The flight track is color coded according to the aircraft altitude; line thickness is proportional to the flight time (the thicker the older).

Distribution of angle of attack values measured by the gust probe on level flight legs suggests that the inlet should be tilted by about 2° (see Figure 31). Interestingly, the angle of attack values are within 1.1° for 90% of the time (of level flight), which is much less than variations of aircraft pitch angle (about 4°; see Figure 32).

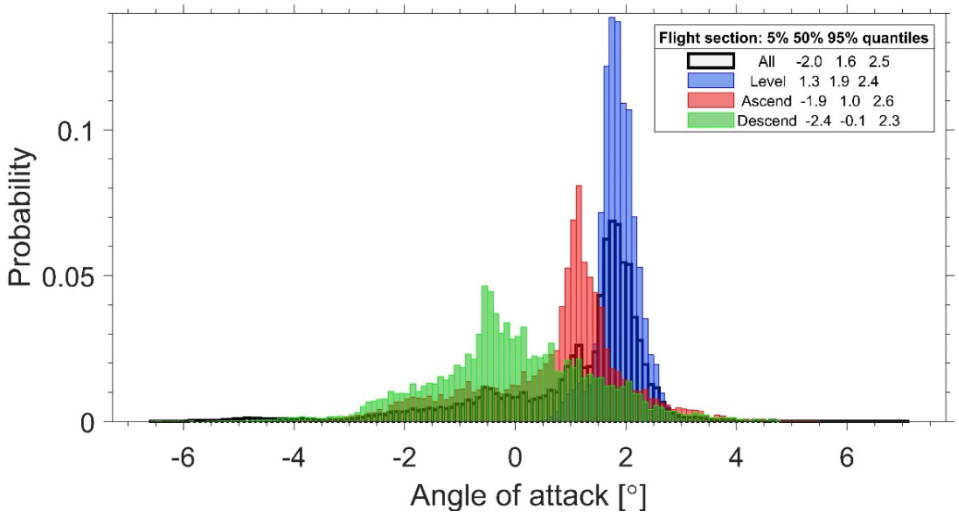

Figure 31. Angle of attack of the incoming flow at the inlet tip position measured by five-port gust probe (AeroProbe). The data were collected in the flight over the ARM SGP site on November 8, 2021. Numbers in the legend show 5%, 50%, and 95% quantiles.

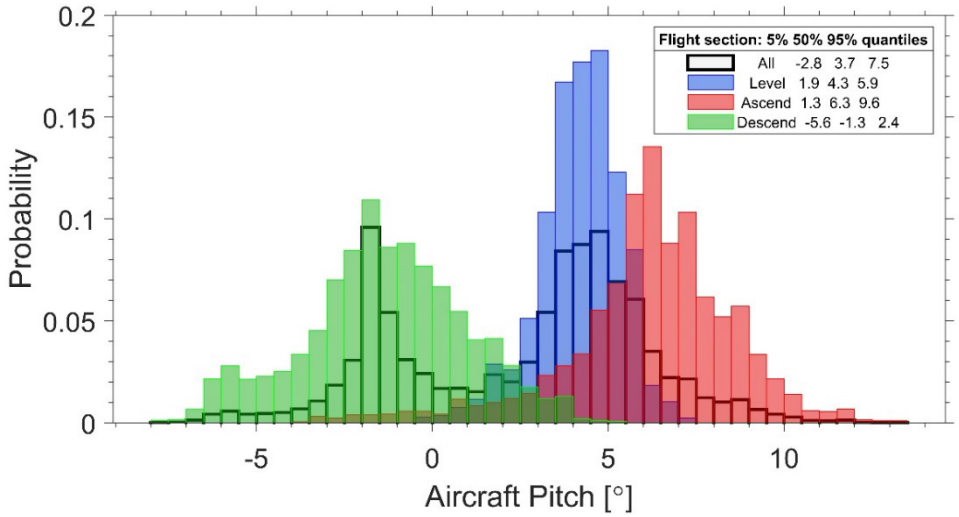

Figure 32. PICOLO (autopilot)-reported aircraft pitch angle. The data were collected in the flight over the ARM SGP site on November 8, 2021. Numbers in the legend show 5%, 50%, and 95% quantiles.

Comparing Figures 31 and 32, it is clear that the aircraft pitch angle is a really poor proxy for the angle of attack – even during nominally level flight platform vertical motion affects AoA, making its variation smaller than pitch angle variations. Generally speaking, this is because the aircrafts fly in the most streamlined way as possible for a dynamic system with substantial mass and inertia moments.

We ran a few comparisons of the gust probe data with AIMMS-30 and autopilot (PICCOLO) data as a sanity check of the gust probe performance (see Figures 33 through 35). Overall, all compared parameters agreed well (correlation coefficients about 0.9). However, we note that comparison of the angle of attack should be treated as a qualitative one since the standard output datastream of the AIMMS-30 does not contain angle of attack per se, but some "AoA pressure difference" values that allowed us to calculate our estimation of angle of attack, similar to what we did in Section 2.5.3.

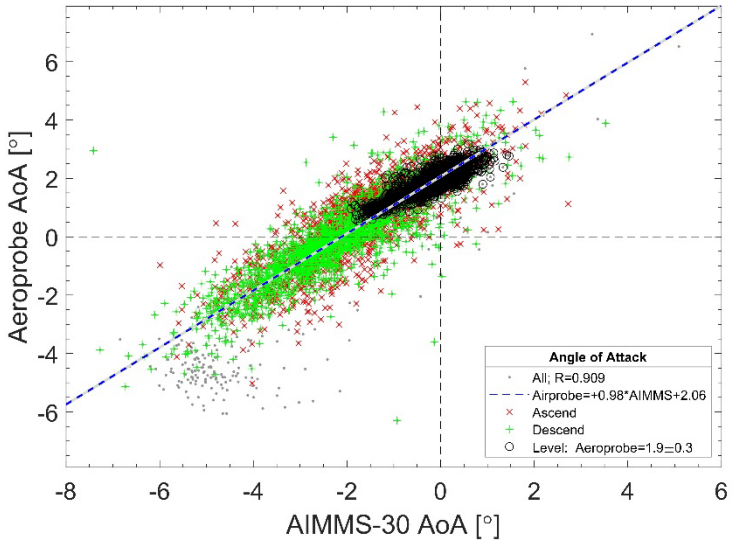

Figure 33. Angle of attack measured by AirProbe versus AoA estimated from AIMMS-30 output. The color of the markers correspond to sections of the flight (November 8, 2021, SGP).

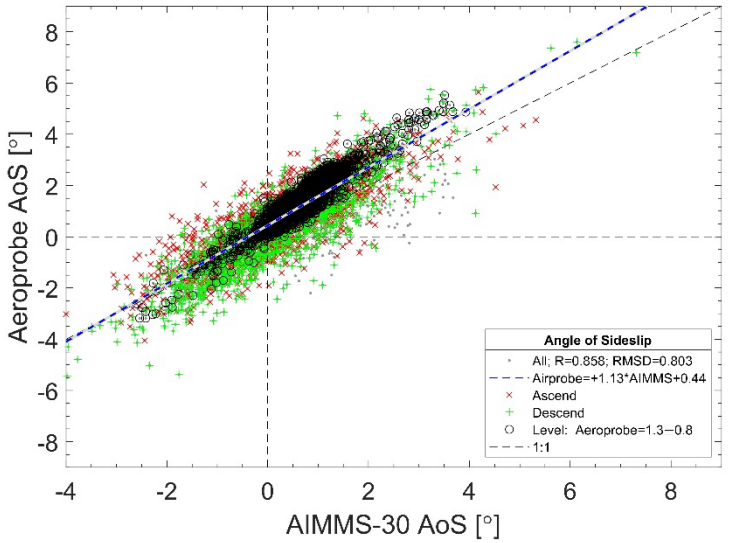

Figure 34. Angle of sideslip measured by AirProbe and AIMMS-30. The color of the markers corresponds to sections of the flight (November 8, 2021, SGP).

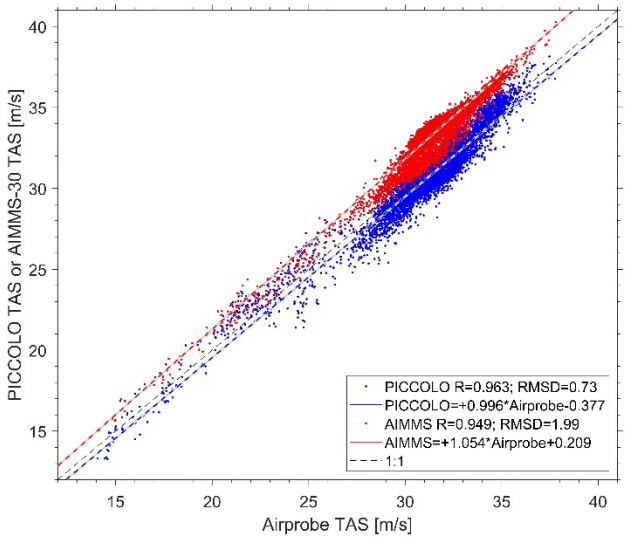

Figure 35. True air speed measured by AirProbe, AIMMS-30, and PICCOLO (aircraft Pitot-static system) during the flight over the SGP ARM Central Facility on November 8, 2021.

3.3.2 Community Aerosol Inlet: Total Flow and Tip Air Speed

The inlet tip air speed V_{tip} was calculated in post-processing from Venturi tube flow measurements corrected for local temperature and pressure. When the Community Aerosol Inlet is operated in constant flow mode, the air speed at the tip is rather stable; its fluctuation is determined by instability of the sample flows of the instruments and the MFC. For example, during the flight on June 23, 2021, the standard deviation of tip air speed was about 0.2 m/s for straight-and-level flight legs (or 90% values are within 0.6m/s; see Figure 36), which corresponds approximately to 0.06 LPM instability in the total inlet flow (0.18 LPM for 90% range coverage). The main contributor to the difference between TAS and tip air speed is TAS's much wider variation range: the standard deviation of TAS is about 0.9 m/s (90% of values are within 2.8 m/s). The deviation of the tip air speed from isokinetic conditions is within ±5% for 90% of the time for straight-and-level flight (see quantiles in the legend in Figure 36), which is better than the ±10% required by the EPA Method 5 for isokinetic sampling.

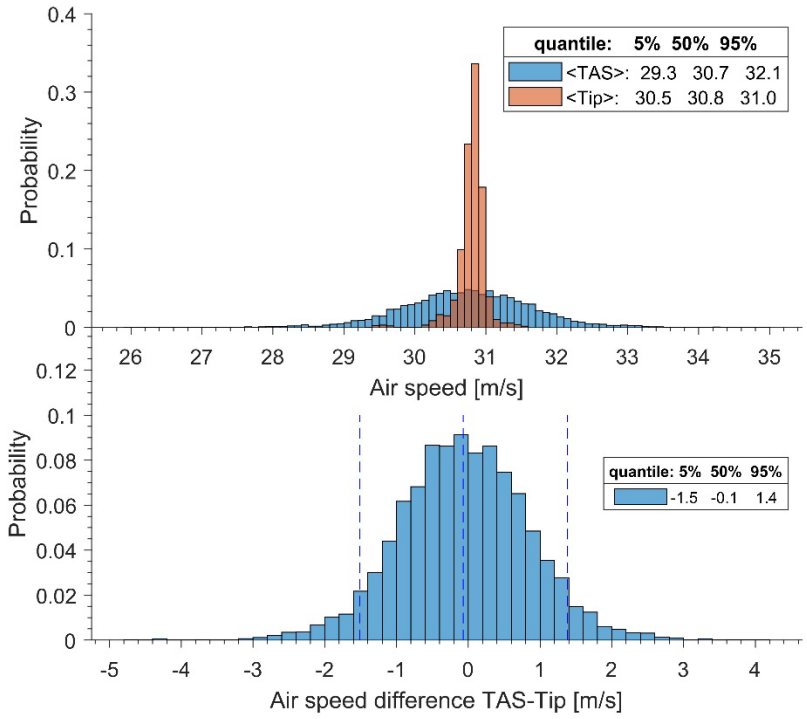

Figure 36. Distribution of TAS, tip air speed, and their difference measured in the flight over Mississippi on June 23, 2021. Numbers in the legend show 5%, 50%, and 95% quantiles.

The tip air speed is determined by the total *volumetric* flow through the inlet. Currently, the total air flow through the inlet is a combination of several contributors, most of which are maintained at constant mass flow (about 7 LPM) and the rest is maintained at constant volumetric flow (about 2 LPM). The total *volumetric* flow F_{tot}, which determines the tip air speed, in this case depends on air density $F_{tot} = F_{sub} + Q_{sub}\,\rho_0/\rho$, where F_{sub} is volumetrically controlled flow fraction, Q_{sub} is mass-controlled flow fraction, and ρ_0 and ρ are standard and local air densities. As the air density drops with altitude, the total volumetric flow increases. The PICCOLO control system flies the aircraft at nominal indicated air speed. The true air speed, corresponding to nominal IAS, increases with altitude as $\sqrt{\rho_0/\rho}$, so both TAS and total inlet flow (or tip air speed) increase with altitude, but at a different rate. If the inlet flow was balanced at the ground to provide isokinetic sampling, at an altitude the inlet gets into a super-kinetic state. For the lowest kilometer this imbalance is not significant, but for higher altitudes it should be corrected by lowering the bypass flow.

Histograms of TAS, tip air speed V_{tip}, and the difference between them for several altitudes measured during the flight over SGP on November 9, 2021 illustrate the altitude dependance of the above parameters (Figure 37).

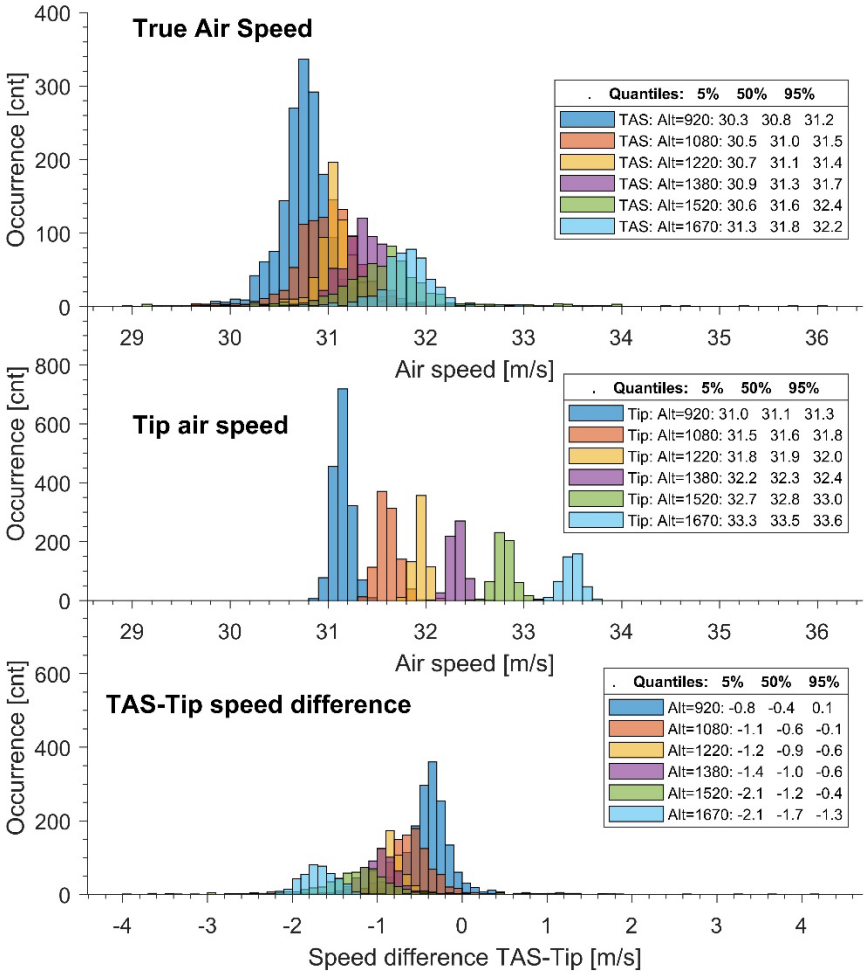

Figure 37. Distribution of TAS, tip air speed, and their difference for several altitudes measured in the flight over the SGP on November 9, 2021. Numbers in the legend show 5%, 50%, and 95% quantiles for specific altitudes.

Even with substantial altitude variation, the tip air speed was within 7% of isokinetic for 90% of flight, excluding initial ascent and final descent (see quantiles in the legends in Figure 37).

Variation of the TigerShark TAS is a direct consequence of how the aircraft is controlled – the auto pilot maintains a certain altitude and indicated air speed mostly by varying engine power (throttle position) between almost full and idle settings; thus, the flight exhibits a continuously undulating pattern ("porpoising", or phugoid), with actual altitude and speed oscillating within certain limits.

We processed the data from the two Mississippi deployments: all straight-and-level legs were divided into "ascent" and "descent" sections, and statistics for IAS, altitude gain or loss, and timing were calculated (Figure 38). "Up" and "down" statistics look almost symmetrical: 90% of IAS variation for "ascents" and "descents" are within 1.1 m/s and 1.3 m/s correspondingly.

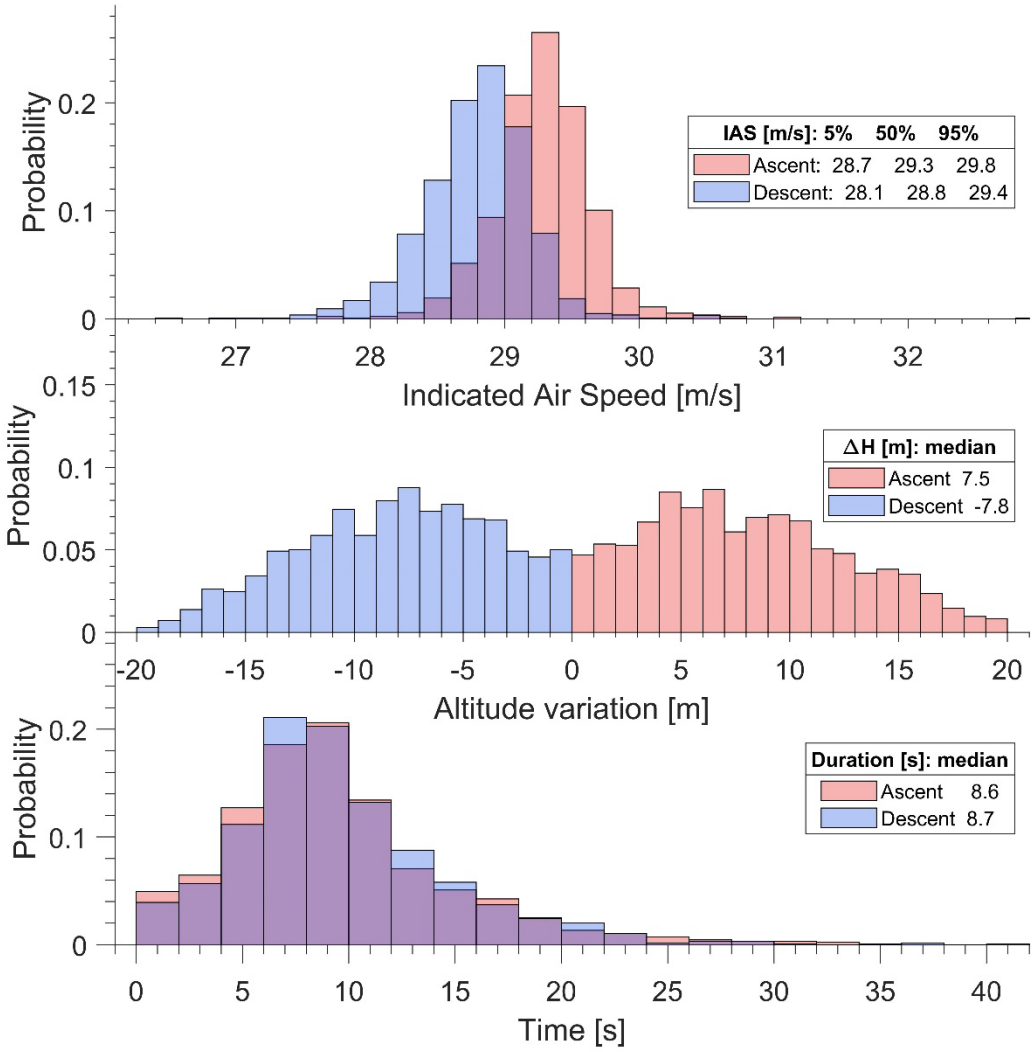

Figure 38. "Porpoising" parameters of the TigerShark flight pattern: distributions of IAS, altitude variation ΔH, and time of undulation for 10 flights during two deployments in Mississippi, March and June 2021. Numbers in the legends show either median values or quantiles for ascent and descent sections.

Our estimate with Particle Loss Calculator (Section 3.2.8, Figure 26) shows that the observed air speed mismatch $\Delta V = TAS - V_{tip}$ should not significantly affect inlet collection efficiency – 95% pass cut size is about 1.5 µm, while 50% is above 11 µm for a worst case of ΔV about -2 m/s.

3.3.3 Sample Air Humidity Conditioning (Drier Performance)

The humidity conditioning sub-system (drier) is based on Nafion single-line, large-bore, 12-inch-long drier model MD-700 (by Perma Pure). We have vast experience, mostly positive, using similar driers of various length on board a manned aircraft in a variety of climates, from arctic (North Slope of Alaska) to tropical (Amazonia, Brazil).

Flight tests over Mississippi in March and June confirmed that the implemented drier is adequate for the task: dew point of the sample was usually lowered by about 8°C and relative humidity after the drier was well below target 40% (Figure 39).

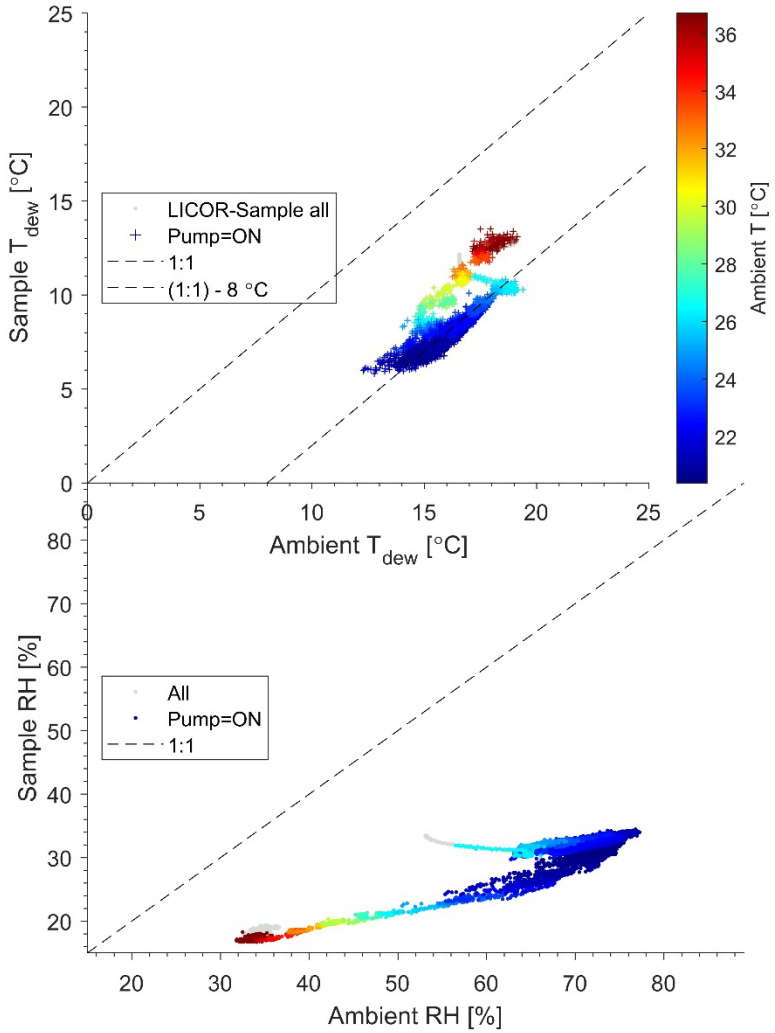

Figure 39. Example of relative humidity and dew point temperature measured by the Licor CO_2/H_2O infrared gas analyzer (ambient) and Sample T/RH sensors during flight in Mississippi on June 23, 2021. The dots are color coded with ambient temperature; gray dots correspond to the data collected when the aerosol pump was not working.

The relative humidity in the sample line after the drier drops due to two processes: removal of the water vapor by the drier and increase of sample air temperature. The TigerShark body is not sealed; it is not pressurized; there is substantial flow of ambient air through the instrument bay; however, the temperature inside the instrument stack in the bay is usually above the ambient by 3 to 7°C (most common value for the Mississippi deployments was about 4°C) due to dissipation of heat by the instrumentation and direct heating of the aircraft body by sunlight. Change in RH values due to water vapor removal (or lower the

dew point temperature) is illustrated by Figure 40, where "dried" air relative humidity is plotted as a function of the air temperature for a fixed drop in the dew point temperature $\Delta T_{dew}=8°C$ and several values of initial RH.

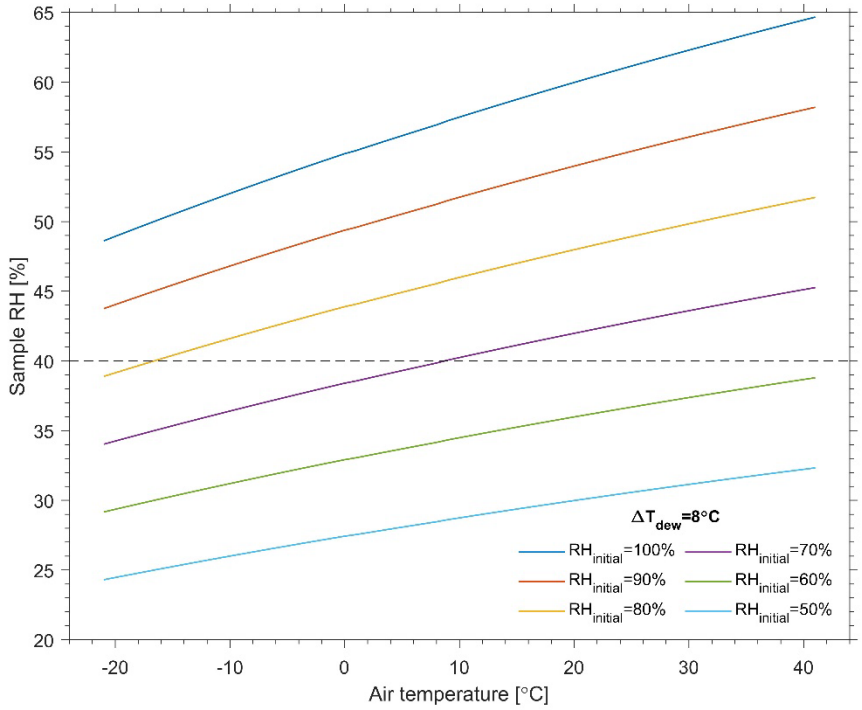

Figure 40. "Dried" air relative humidity calculated as a function of air temperature for a fixed drop in dew point temperature (ΔT_{dew}=8°C) and several values of initial relative humidity.

Clearly, just vapor removal cannot achieve the target 40% RH level for the whole temperature range when initial relative humidity is above 60%. Figure 41 shows an estimate of sample air relative humidity calculated for drop in dew point temperature $\Delta T_{dew}=8°C$ and increase in air sample temperature up to $\Delta T=4°C$ for several initial relative humidity levels. Shaded areas are bordered by RH lines calculated for $\Delta T=0°C$ (upper border) and $\Delta T=4°C$ (lower border).

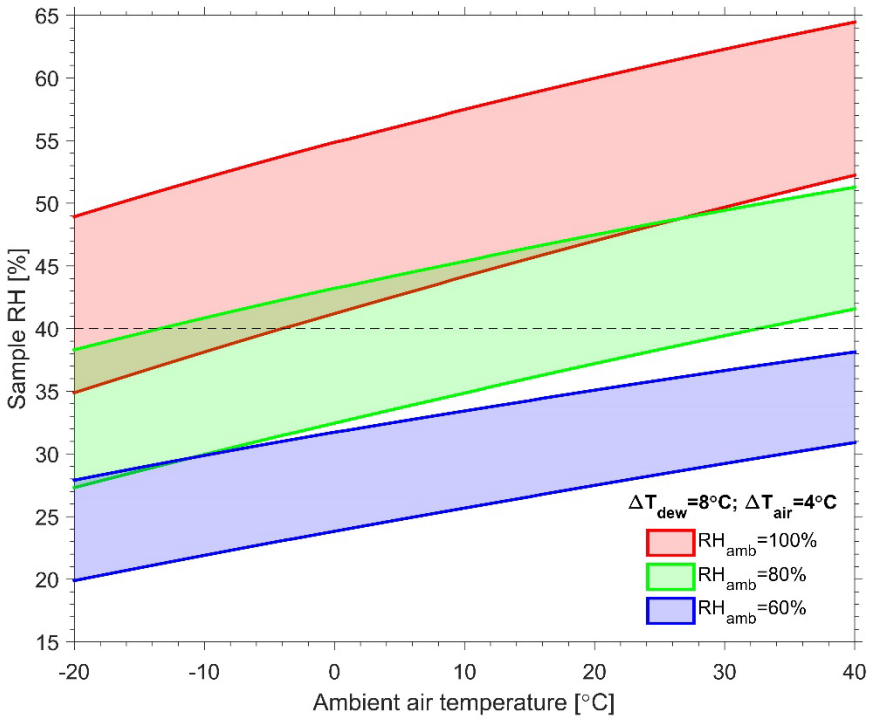

Figure 41. Sample air relative humidity calculated as a function of ambient air temperature for several values of initial RH, a fixed drop in dew point temperature ΔT_{dew}=8°C, and increase in the sample air temperature up to 4°C. The "shaded" areas are bordered by RH lines calculated for ΔT=0°C (upper border) and ΔT=4°C (lower border).

If we will be deploying in a more hot and humid location than summertime Mississippi, we can easily replace the current 12-inch unit with an 18- or 24-inch unit to provide additional drying.

3.4 Concluding Remarks and Future Improvements

The designed Community Aerosol Inlet met or exceeded requirements, as demonstrated in flight tests.

Next steps of the inlet development would be:

- Adding designated sensors to measure temperature and total pressure in the Venturi tube to correct flow readings for air density variation in real time.
- Acquiring additional experience and real-world data for analysis of inlet performance and deficiencies.
- Choice of main operational mode: constant flow with manual altitude adjustment or TAS tracing.
- Development of the "controller" – either a controlling program running on the main DAQ computer or a dedicated microcontroller and user interface program on the DAQ or MOC computer.
- Lower weight and power consumption of the inlet by:
  - Replacement of the bypass MFC with an automated butterfly valve.

  - Replacement of the current vacuum pump with a scarf device for the major part of the inlet air flow and a smaller vacuum pump capable of handling just the flows for the pumpless instrumentation.
- Minimize linear dimensions of the inlet – the Venturi tube might be implemented as an insert to the back end of the main inlet tube.
- Find a set of sensors, required by the inlet, with a common communication protocol (e.g., I2C) instead of the current collection of RS-232, analog, etc.

4.0 Conclusions

This report presents designs of two aerosol inlets suitable for a medium-sized UAS. The report shows all steps, reasons, formulas, and internal logics for choice of the initial parameters and physical sizes and for subsequent refining of the design; the report contains sufficient details so that both inlets can be customized by qualified engineers for specific sampling and/or deployment requirements.

One of the described inlets is a specialized inlet for a miniaturized aerosol spectrometer (POPS). The inlet is designed to be mounted in a pylon; however, it could be mounted in the aircraft body with minimal changes. The main advantages of this inlet are:

- Passive, needs no power or control to operate; current implementation incorporates a flow meter to fine tune it and monitor the inlet performance
- Self-adjusting in terms of maintaining the isokinetic sampling through the tip in spite of variation of the incoming air speed in a wide range
- Minimal distortion to the sample air and aerosol population
- Simple construction, could be 3D printed, machined, or manufactured in “mixed” style
- Flexible design, can be easily adapted for a different platform and/or instrumentation
- Basic relative humidity control via sample temperature manipulation (heating) can be easily incorporated (will require additional power)
- Lightweight
- Inexpensive.

The inlet has several limitations:

- The sample flow going to the instrumentation should constitute a small fraction of the total inlet flow.
- Isokinetic sampling at the instrument pickoff is achievable only at one platform speed. The inlet maintains isokinetic sampling at the tip for wide range of the incoming air speed, but it does not maintain constant air flow/speed inside the inlet main tube, where instrument pickoff is mounted. However, this disbalance should not significantly affect aerosol collection efficiency since the air speed inside the main tube is low.
- Complete adaptation to a different cruise speed requires a change in physical dimensions of the inlet (inlet tip orifice and/or main tube ID) and new fine tuning (selection of the correct flow-resisting element in several test flights).

- Implementation of humidity control based on water vapor removal out of the sample air (drying) will require the addition of bulky and heavy parts.

After the POPS sensor was incorporated into the PNNL standard aerosol payload and moved into the aircraft instrumentation bay, the design of the pylon-mounted inlet was placed on hold.

The second described inlet, called Community Aerosol Inlet, is an actively controlled isokinetic inlet designed to work with a suite of heterogeneous instrumentation with diverse requirements for the sample air distribution and conditioning. An efficient humidity conditioning system (drier) is incorporated into the inlet to maintain aerosol sample relative humidity at a low enough level (recommended 40% or below) so that aerosol may be considered to be in "dry" state. The inlet contains few specially manufactured parts (front cone and Venturi tube); all other parts are easily available, off-the-shelf commercial products.

The main advantages of this inlet are:

- Flexible design that allows:
  - Operation in two modes: constant flow and TAS tracing
  - Easy adaptation to different platform and/or suit of instruments mostly by re-adjusting settings and/or software; may not require replacement of the inlet parts
- Humidity conditioning sub-system
- Vacuum source to accommodate pumpless instrumentation
- Limited operation is possible without human control or main DAQ computer.

This inlet has several limitations:

- Current implementation requires running three separate programs on the main DAQ computer to monitor, control, and record the data; altitude adjustments have to be done by the operator via remote access to the DAQ computer.
- Relatively high power consumption (manly due to the powerful vacuum pump) and, consequently, heat release in the instrument bay.
- Currently, the sensors used in the inlet require diverse data acquisition/communication protocols – serial, analog, I2C − which complicates software/hardware arrangements.

Both inlets have been tested in flight and showed expected performance. Generally, experimental data agree well with our theoretical estimates, which justifies application of the developed approaches for inlet modifications and fine tuning.

5.0 References

Balkanski, Y, M Schulz, T Claquin, and S Guibert. 2007. "Reevaluation of mineral aerosol radiative forcings suggests a better agreement with satellite and AERONET data." *Atmospheric Chemistry and Physics* 7: 81–95, https://doi.org/10.5194/acp-7-81-2007

Baron, PA, and K Willeke. 2001. *Aerosol Measurement: Principles, Techniques and Applications*, 2nd edition. Wiley-Interscience, New York, New York, p. 72.

Barri, M, GK El Khoury, HI Andersson, and B Pettersen. 2010. "DNS of backward-facing step flow with fully turbulent inflow." *International Journal for Numerical Methods in Fluids* 64(7): 777−792, https://doi.org/10.1002/fld.2176

Baumgardner, D, JL Brenguier, A Bucholtz, H Coe, P DeMott, TJ Garrett, JF Gayet, M Hermann, A Heymsfield, A Korolev, M Krämer, A Petzold, W Strapp, P Pilewskie, J Taylor, C Twohy, M Wendisch, W Bachalo, and P Chuang. 2011. "Airborne instruments to measure atmospheric aerosol particles, clouds and radiation: A Cook's tour of mature and emerging technology." *Atmospheric Research* 102(1-2): 10−29, https://doi.org/10.1016/j.atmosres.2011.06.021

Chen, L, K Asai, T Nonomura, G Xi, and T Liu. 2018. "A review of backward-facing step (BFS) flow mechanisms, heat transfer and control." *Thermal Science and Engineering Progress* 6: 194−216, https://doi.org/10.1016/j.tsep.2018.04.004

Ciampi, M, S Faggiani, W Grassi, G Tuoni, and FP Incropera. 1987. "Mixed convection heat transfer in horizontal, concentric annuli for transitional flow conditions." *International Journal of Heat and Mass Transfer* 30(5): 833−841, https://doi.org/10.1016/0017-9310(87)90003-2

Gao, RS, H Telg, RJ McLaughlin, SJ Ciciora, LA Watts, MS Richardson, JP Schwarz, AE Perring, TD Thornberry, AW Rollins, MZ Markovic, TS Bates, JE Johnson, and DW Fahey. 2016. "A light-weight, high-sensitivity particle spectrometer for PM2.5 aerosol measurements." *Aerosol Science and Technology* 50(1): 88–99, https://doi.org/10.1080/02786826.2015.1131809

Gysel, M. M Laborde, JS Olfert, R Subramanian, and AJ Gröhn. 2011. "Effective density of Aquadag and fullerene soot black carbon reference materials used for SP2 calibration." *Atmospheric Measurement Techniques* 4(12): 2851–2858, https://doi.org/10.5194/amt-4-2851-2011

Idelchik, IE. 2007. *Handbook of Hydraulic Resistance,* 4th Edition, Begell House, Danbury, Connecticut. ISBN: 978-1-56700-251-5 (based on Russian edition: *Идельчик.И.Е. Справочник по гидравлическим сопротивлениям*. Москва, Машиностроение, 1992).

ISO 5167-4:2003. *Measurement of fluid flow by means of pressure differential devices inserted in circular cross-section conduits running full — Part 4: Venturi tubes*.

Kesavan, J, and R Doherty.2000. Density Measurements of Materials Used in Aerosol Studies. Report ECBC-TN-003. Edgewood Chemical Biological Center, Aberdeen Proving Ground, Maryland. Available from https://apps.dtic.mil/sti/citations/ADA384063

Landau, LD, and EM Lifshitz. 1959. *Course of Theoretical Physics, Volume 6: Fluid Mechanics*. Translated from Russian by JB Sykes and WH Reid. Pergamon Press, Oxford, United Kingdom.

Liu, PSK, WR Leaitch , JW Strapp, and MA Wasey. 1992. "Response of Particle Measuring Systems Airborne ASASP and PCASP to NaCl and Latex Particles." *Aerosol Science and Technology* 16(2): 83−95, https://doi.org/10.1080/02786829208959539

Mahowald, N, S Albani, JF Kok, S Engelstaeder, R Scanza, DS Ward, and MG Flanner. 2014. "The size distribution of desert dust aerosols and its impact on the Earth system." *Aeolian Research* 15: 53−71, https://doi.org/10.

Mei, F, G McMeeking, M Pekour, RS Gao, G Kulkarni, S China, H Telg, D Dexheimer, J Tomlinson, and B Schmid. 2020. "Performance Assessment of Portable Optical Particle Spectrometer (POPS)." *Sensors (Basel)* 20(21): 6294, https://doi.org/10.3390/s20216294.

Nash, JF, VG Quincey, and J Callinan. 1966. Experiments on Two-Dimensional Base Flow at Subsonic and Transonic Speeds. Ministry of Aviation, Aeronautical Research Council Reports and Memoranda No. 3427, January 1963. Her Majesty's Stationary Office, London, United Kingdom (http://naca.central.cranfield.ac.uk/reports/arc/rm/3427.pdf or https://reports.aerade.cranfield.ac.uk/handle/1826.2/4011).

Ndenguma, DD, J Dirker, and JP Meyer. 2017. "Heat transfer and pressure drop in annuli with approximately uniform internal wall temperatures in the transitional flow regime." *International Journal of Heat and Mass Transfer* 111: 429−441, https://doi.org/10.1016/j.ijheatmasstransfer.2017.02.064

U.S. Environmental Protection Agency. 2016. Method 5 − Particulate Matter (PM), https://www.epa.gov/emc/method-5-particulate-matter-pm or https://www.gpo.gov/fdsys/pkg/FR-2016-08-30/pdf/2016-19642.pdf

von der Weiden, S-L, F Drewnick, and S Borrmann. 2009. "Particle Loss Calculator – a new software tool for the assessment of the performance of aerosol inlet systems." *Atmospheric Measurement Techniques* 2(2): 479–494, https://doi.org/10.5194/amt-2-479-2009. Available from Max-Planck Institute for Chemistry: https://www.mpic.de/4230607/particle-loss-calculator-plc

Wilcox, JD. 1956. "Isokinetic Flow and Sampling." *Journal of the Air Pollution Control Association* 5:4: 226−245, https://doi.org/10.1080/00966665.1956.10467715

World Meteorological Organization/Global Atmosphere Watch Program. 2016. Aerosol measurement procedures, Guidelines and Recommendation. Report No. 227. https://wmo-gaw-sag-aerosol.org/files/FINAL_GAW_227.pdf

www.arm.gov

U.S. DEPARTMENT OF
ENERGY

Office of Science